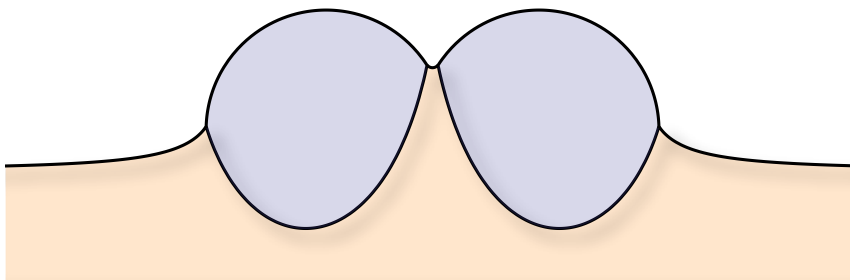


MSc. THESIS APPLIED PHYSICS

L.A. Lubbers

Liquid drops on soft solids



November 8, 2013

Committee:

Prof. Dr. J.H. Snoeijer
Prof. Dr. D. Lohse
Dr. Ir. J.H. Weijs
Prof. Dr. W.J. Briels

Physics of Fluids, Faculty TNW
University of Twente

Abstract

A sessile drop can elastically deform a substrate by the action of capillary forces. The typical size of the deformation is given by the ratio of surface tension and the elastic modulus, γ/E , which can reach up to 10-100 microns for soft elastomers. In this report we theoretically show that the contact angles of drops on such a surface exhibit two transitions when increasing γ/E : (i) the microscopic geometry of the contact line first develops a Neumann-like cusp when γ/E is of the order of few nanometers, (ii) the macroscopic angle of the drop is altered only when γ/E reaches the size of the drop. Using the same framework we then show that two neighboring drops exhibit an effective interaction, mediated by the deformation of the elastic medium. This is in analogy to the well-known Cheerios effect, where small particles at a liquid interface attract each other due to the meniscus deformations. We find that drop-drop interactions have both an attractive and repulsive regime depending on their separation distance, with the typical cross-over from attractive to repulsive taking place at a separation of a few drop diameters.

Contents

1	Introduction	3
1.1	Elasto-capillarity	3
1.2	Drop motion	6
1.3	Thesis outline	7
2	Formalism	9
2.1	Elasticity and capillary tractions	9
2.2	Mechanical equilibrium through variational calculus	11
2.2.1	Variation of the liquid interface: $\mathcal{H}(x)$	13
2.2.2	Variation of the elastic interface: $h(x)$	15
2.2.3	Closure of the problem through the contact angle θ	16
2.3	Solving the equations	16
3	Single Sessile Drop	19
3.1	Surface deformations due drop presence	19
3.1.1	Two dimensional drop	19
3.1.2	Axisymmetric drop	22
3.1.3	Asymptotics	24
3.2	From rigid to soft: Two transitions of the contact angles	27
3.2.1	Is surface tension perfectly localized?	27
3.2.2	Geometry of the contact line as function of softness parameter	29
3.3	Free energy as function of the softness parameter	31
3.4	Summary	33
4	Drop Interactions	34
4.1	Extending the single drop model	34
4.2	Presence of a second drop: A non-equilibrium state	37
4.2.1	A thought experiment: Fixing the drop separation ℓ	37
4.2.2	The liquid shape $\mathcal{H}(x)$ for asymmetric drops	39
4.3	Numerical results	43
4.4	Summary	45
5	Discussion and Outlook	47
5.1	Discussion	47
5.2	Outlook	48
A	Liquid cap equations	49
A.1	Spherical cap single drop	49
A.2	Relating θ_{in} to θ_{out} for contact line pinning	50
B	Energy integrals	51
B.1	Elastic energy	51
B.2	Solid surface capillary energy	52

Chapter 1

Introduction

1.1 Elasto-capillarity

Anyone wearing soft contact lenses will have noticed a drop of contact lens solution can deform the lens whilst cleaning it. Here, the lens gets deformed under the action of capillary forces induced by the drop. Both the equilibrium shape of the lens and drop are determined by the complex, often non-linear, interplay between capillary forces and the elastic response of the lens, thereby referred to as *elasto-capillary* interactions [1]. Even though these elasto-capillary interactions might be undesirable during the cleaning process of contact lenses, these interactions are taken advantage of in the biological world by, for example, the flexible legs of water striders [2, 3]. Moreover, elasto-capillary interactions are not only limited to biological systems, but also have applications in industry, for example during the folding and assembly of planar materials [4, 5, 6].

An illustration of elasto-capillary effects is given in Fig. 1.1(a), where the folding and bending of a triangular and flower-like shaped elastic sheet after depositing a water droplet is shown. Bending of the elastic sheet can be explained from an energetical point of view: Curving the sheet reduces the liquid-vapor interface area and thus the liquid surface energy. This happens at the expense of

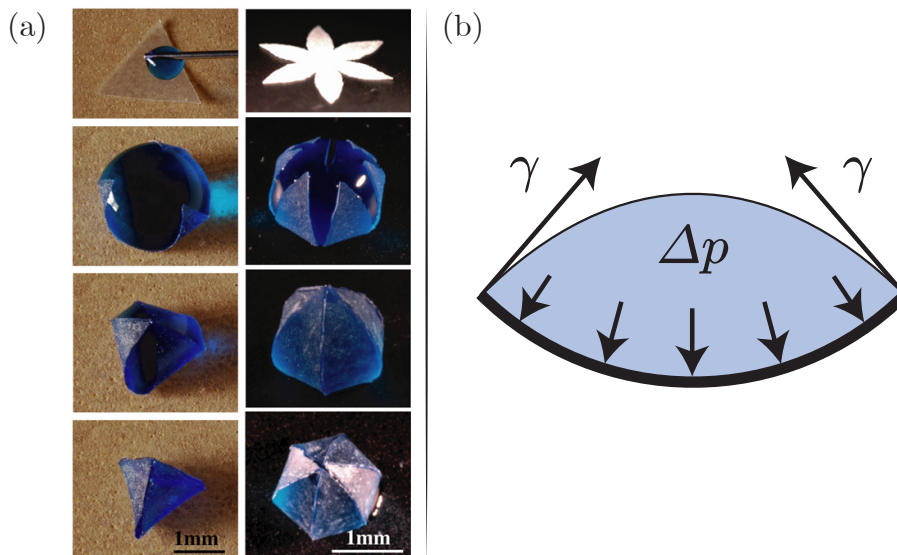


Figure 1.1: Spontaneous self wrapping of elastic sheets around a droplet of water and schematics of capillary forces on the elastic sheets. (a) Deposition of a water droplet on a PDMS (left) and silicon sheet (right) bends the elastic sheets under the action of capillary forces. The bending process continues and wraps the elastic sheet during drop evaporation. Image sequence taken from [4]. (b) Schematic representation of (2-D) capillary forces on the solid. The liquid surface tension γ pulls on the edges of the sheet, while the Laplace pressure (Δp) in the drop is pushing down the sheet.

an increase in elastic energy, leading to an equilibrium configuration. Alternatively, this may be explained from a mechanical perspective by considering the action of capillary forces, sketched in Fig. 1.1(b). Surface tension of the liquid pulls the sheet around the drop volume and the Laplace pressure, Δp , pushes down on the sheet, resulting in bending of the sheet. The work shown in Fig. 1.1, including many others, focuses on the shaping of soft, slender surfaces by surface stresses originating from the liquid surface tension [7, 8, 9]. In these cases the deformation is primarily observed through bending of these slender bodies.

In this thesis, however, we do not consider slender bodies. Rather, we consider liquid drops on thick, soft solid surfaces as sketched in Fig. 1.2(a). In the case of substrates being both thicker and wider (with respect to the drop radius), bending is taken over by stretching and compression of the soft solid. These deformations manifest themselves on smaller scales and hence are less apparent. They are nonetheless present, and ongoing efforts have been made on the stretching and compressing of soft solids in the last years [10, 11, 12, 13, 14, 15, 16]. In particular, consider the case shown in Fig. 1.2(b). It shows a fluorescent ionic drop on an elastic PDMS surface, imaged by laser scanning confocal microscopy [10]. Clearly, the elastic substrate is lifted in the direct vicinity of the contact lines and the Laplace pressure at the center is pushing down the substrate [Fig. 1.2(a-b)], revealing a similar mechanism as the bending sheet [Fig. 1.1(b)]. While these deformations are driven by capillary forces, γ , the solid is resisting them due a finite elastic modulus, E . This naturally leads to the typical length-scale of deformations [1, 7, 11]:

$$\Delta h_{ec} \approx \frac{\gamma}{E}. \quad (1.1)$$

The ratio γ/E has units of length, and is known as the *elasto-capillary* length. It describes the competition between capillary and elastic forces, in contrast to the capillary length which compares capillary and gravitational forces [1]. On very soft solids the elasto-capillary length can reach up to 100 microns and the order of these deformations allow themselves to be measured in experiments [10, 12, 16]. Typically, however, the elasto-capillary length is on the order of a few Å. For example, a water drop deposited on a glass plate ($\gamma = 69 \times 10^{-3}$ N/m, $E = 69 \times 10^6$ Pa) has an elasto-capillary length $\Delta h_{ec} \sim 10^{-9}$ m = 1Å, and is thus limited to the molecular scale. Deformations at the sub-molecular scale have previously been measured in molecular dynamics (MD) simulations [Fig. 1.2.(c)], yielding deformations of 1/1000 of an atom diameter around the contact line [11].

MD simulations as mentioned above approach the problem from a *microscopic* point of view:

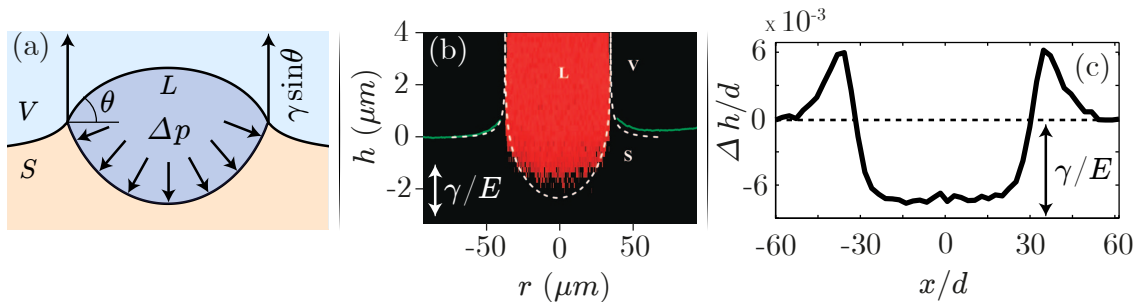


Figure 1.2: A sessile drop on a soft solid: schematics, experiments and molecular dynamics (MD) simulations. The solid is lifted in the periphery of the contact lines due the vertical liquid-vapor (LV) tension component, and pushed downwards due the Laplace pressure in the center of the drop. In both (b) and (c) $h = 0$ corresponds to the undisturbed surface profile before droplet presence and the arrow denoted γ/E equals the elasto-capillary length Δh_{ec} . (a) Schematics of a sessile drop on a soft solid. Vertical components of the LV tension are lifting the substrate at both contact lines, while the Laplace pressure counteracts this force by pushing down on the substrate. (b) Experimental visualization of a fluorescent drop ($\gamma = 48.8 \times 10^{-3}$ N/m) on an elastic PDMS surface ($E = 25$ kPa), using laser scanning confocal microscopy. Filled red regions expose the liquid drop, having a contact radius of $33.5 \mu\text{m}$, and the green line displays the free surface. Note the aspect ratio of the image has been highly stretched in vertical direction. Image adapted from [10]. (c) MD results for deformations of a drop ($\gamma = 3.1 \times 10^{-2}$ N/m) on a substrate with a high elastic modulus, $E = 11 \times 10^9$ Pa, where d is the molecular diameter. Even though the resulting elasto-capillary length is on the order of sub-Å, deformations can be measured in MD after averaging out thermal fluctuations over a time window. Both contact lines are located at $x \approx \pm 35d$. Image adapted from [11].

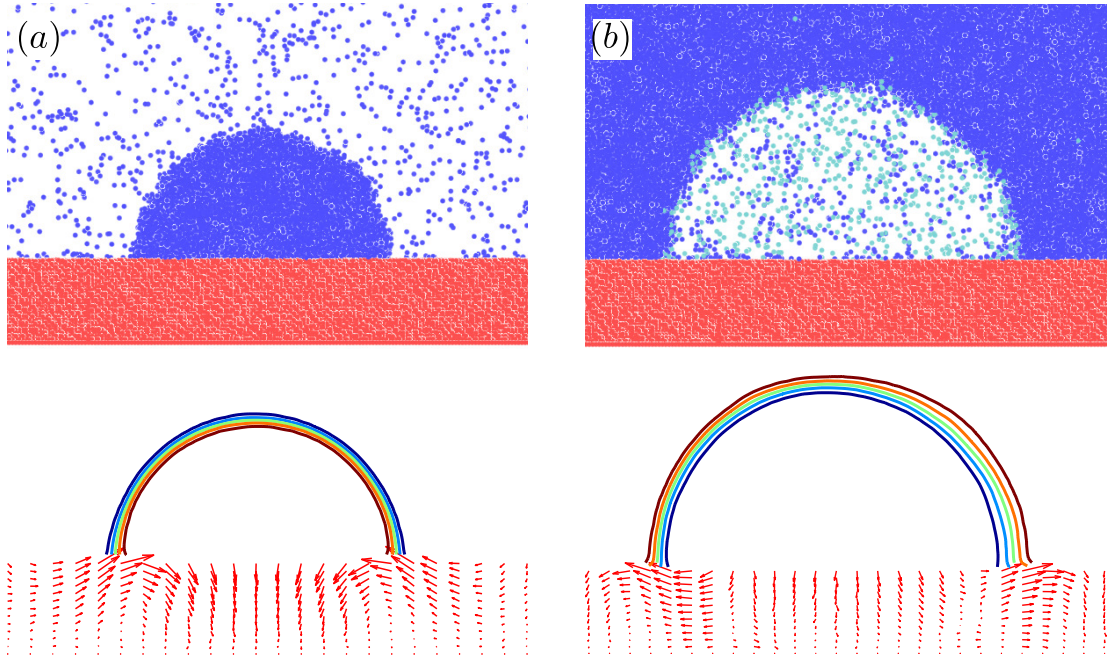


Figure 1.3: Molecular dynamics simulations of a drop (a) and bubble (b) on a soft (compressible) solid, by Weijs *et al* [11, 17]. In both the drop and bubble have $\gamma_{SV} = \gamma_{SL}$, such that the contact angle is 90° . Top figures show snapshots from these simulations: Red, blue and cyan particles display solid, liquid and gas atoms respectively. Bottom figures show local displacements of the soft solid (red arrows). Liquid density contours (rainbow colours), indicate the respective locations of the drop and bubble with respect to the solid. (a) Drop on a soft solid. The presence of the drop induces local displacements in the solid. Note how the solid is stretched in the vicinity of the contact lines, and compressed inside the drop, similar to the picture sketched in Fig 1.2. Furthermore these simulations shows the soft solid exhibits tangential displacements near the contact line. (b) Bubble on a soft solid. The presence of the bubble induces displacements in the solid. As for the drop, the solid is stretched near the contact lines, compressed inside the drop, but tangential displacements have reversed its direction.

roughly speaking, it only assumes an effective interaction potential between atoms, which allows elastic effects to be studied without requiring a macroscopic description of the elastic problem. MD also allows for accurate measurements of displacements in the soft solid. A completer picture is provided in Fig. 1.3, clearly illustrating that apart from normal displacements, the soft solid also exhibits tangential displacements around the contact line [11, 17]. One could argue these tangential displacements are simply caused by the elastic response of the soft solid to the Laplace pressure pushing down on the substrate: In this case this is not true, however, since the direction of tangential displacements are reversed in case of the drop [Fig. 1.3(a)] and bubble [1.3(b)]. Instead, tangential displacements have been shown to be caused by a tangential force below the contact line [13, 18, 17] that is always directed towards the liquid phase, which we name f_t .

A drawback of this microscopic approach is that it is computationally time consuming while it is limiting the maximum length scale involved in the problem at the same. Therefore we choose to approach the problem from a macroscopic point of view in this thesis. In doing so, we will consider normal forces f_n only, and ignore tangential forces, that is, $f_t = 0$. Choosing $f_t = 0$ is a good starting point, because it is able to capture the main physics, while it circumvents difficulties associated with these tangential forces. Preliminary results have shown this assumption to be valid in the case of an incompressible solid [11]. Typically, extremely soft solids used in experiments are gel-like, which are also incompressible [12, 16, 19]. The macroscopic approach used in this thesis couples the action of capillary forces to continuum linear elastic theory [12, 13, 14]. So far, theoretical models using the macroscopic framework for a single drop on a soft solid have been compared with reasonable agreement against experimental results [12, 20]. Jerison *et al.* [12] demonstrated that the good agreement was only possible by accounting for the free energy of the solid surface, acting as an additional stress due to the curvature of the solid. Recent experiments have shown that a solid indeed can have a surface free energy γ_S : A thin filament of gel was

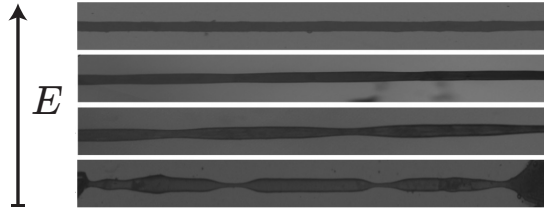


Figure 1.4: Experimental evidence of soft solids carrying surface energy through a gel that exhibits a Rayleigh-Plateau-like instability [21]. A thin, cylindrically shaped filament of agar gel, having a radius of $240 \mu\text{m}$ becomes unstable for decreasing elastic modulus E in order to decrease its surface energy. The finite elasticity of the gel prevents the break up in separate "drops". Image adapted from [22].

observed to exhibit a Rayleigh-Plateau-like instability [21, 22], shown in Fig. 1.4. In classical fluid dynamics, the Rayleigh-Plateau instability occurs because a liquid filament lowers its total surface energy by breaking up in separate liquid droplets. Analogously, one could explain the formation of clusters of gel in Fig. (1.4) by a similar energy argument, suggesting the solid carries a solid surface tension. Even though out-of-plane as well as in-plane deformations have been described by this theoretical framework taking into account the solid surface tension, one of the most basic characterizations of wetting on soft solids remains unanswered: What is the contact angle θ a liquid drop makes on a soft solid, and which dimensionless parameters govern its value? More specifically, since γ/E is the relevant length scale of deformations, to what other length scale should it be compared to characterize θ ? Is that the macroscopic length scale of the drop, R_0 , the microscopic length scale of molecular interactions, a , or any other relevant length scale? These will form the central questions in chapter 3 of this report.

1.2 Drop motion

Other than the static case of a single liquid drop wetting a soft solid, drops have been shown to exhibit dynamical behaviour on specific substrates, such as substrates having temperature, wettability or stiffness gradients [1, 23, 25]. Similar mechanisms have been observed for living cells, utilizing stiffness gradients as movement guidance [26, 27]. This guiding mechanism, known as durotaxis in the biological world, can be driven by both a gradient in elastic modulus or by a gradient in substrate thickness: Both cause a gradient of stiffness in the substrate. An illustration of this effect is shown in Fig. 1.5, which shows two images of experiments for droplets deposited on a substrate of variable thickness, the dark bands being the thickest regions. Style *et al.* [23] observed movement of these drops predominantly oriented towards these dark bands. They argued

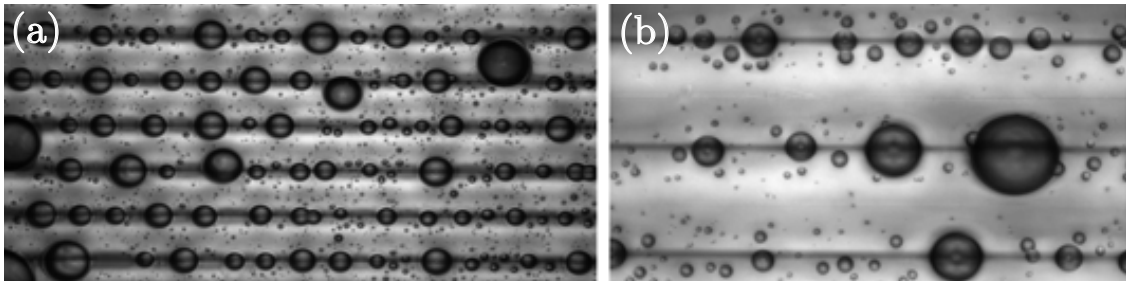


Figure 1.5: Spontaneous movement of droplets under the influence of durotaxis. (a,b) Droplets can move on a soft solid having a stiffness gradient, such as a variable substrate thickness. Here the substrate has a periodic thickness gradient, the dark horizontal bands are located at the thickest regions of the silicon gel substrate. The spacing between the bands is $170 \mu\text{m}$. After depositing glycerol droplets on the soft substrate, they were observed to move predominantly in the direction of the dark bands under the influence of durotaxis: Image (b) shows the drop distribution 5 minutes after deposition, (zoomed) image (c) after 5 hours. Image taken from [23].

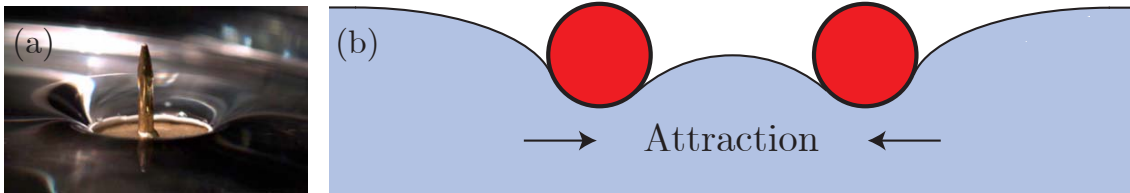


Figure 1.6: (a) Image of a drawing pin floating upturned on water. Note how the liquid interface is deformed in order to counterbalance the weight of the pin. Image taken from [24]. (b) Deformations of the liquid interface caused by the presence of *two* particles at that interface can lead to mutual attraction. Both particles deform the liquid interface by their weight, thereby creating a local perturbation in the environment of one another. This perturbation does not allow for an intermediate equilibrium state [as was possible for a single particle, depicted in (a)], leading to a mutual interaction of the particles, causing the particles to move.

drops preferably reorganized themselves in the vicinity of thick regions, because drops appeared to wet thick substrates more strongly than thin substrates (lower contact angle), thereby leading to a reduction in interfacial energy. In other words, movement towards the dark bands causes the drop shape to change, leading to a decrease in interfacial energy, driven by the substrate's stiffness gradient. This analysis, however, does not take into account that also the bulk elastic energy varies. In fact, this contribution promotes drop movement towards the *stiffer* region of the substrate and *a priori* it is unclear which of the two mechanisms dominate.

In addition to movement oriented towards the dark bands Jerison *et al.* reported coalescence of droplets oriented along the dark bands. Even though movement of drops oriented towards the dark bands can be attributed to the stiffness gradient, movement in directions parallel to the dark bands cannot, because the substrate thickness is invariant in that direction. A plausible explanation for the observed coalescence is that it is driven by drop-drop interaction forces through the elastic substrate: This raises the intriguing prospect of *elastic interactions*, mediated by the elastic deformations of the solid. This is analogous to the well-known Cheerios effect, where small particles at a liquid interface attract each other due to the meniscus deformations [24, 28]. In fact, many people are daily unwittingly dealing with this effect when having breakfast: Cheerios cereals mixed with milk attract each other at the milk interface, explaining the origin of the name "Cheerios-effect" [24].

Fig. 1.6 sketches the underlying mechanism of the Cheerios effect: The liquid interface deforms in order to counterbalance the weight of a particle such that it floats at the interface, Fig. 1.6(a). These deformations create a local perturbation of the liquid interface on any other particle being in the vicinity, thereby inducing a mutual force, or equally, an energy gradient Fig. 1.6(b). This mutual interaction between particles can cause movement and eventually aggregation of particles. Inspired by the Cheerios effect, we expect a similar mechanism for drops on soft solids. In this case it is the solid interface (vs liquid interface for Cheerios) that is elastically deformed under the action of capillary forces: Elastic deformations caused by drop 1, are felt by drop 2, and the other way around, causing mutual interaction between these drops. Although dynamical behaviour driven by durotaxis or liquid meniscus deformations (Cheerios) has been investigated to a certain extent, much less is known about elastic drop-drop interactions on a soft substrate. Can we describe these elastic drop-drop interactions, what is its magnitude, and what is the underlying physical mechanism driving these interactions? These will be the key questions remain to be answered in chapter 4.

1.3 Thesis outline

In this thesis we develop a macroscopic framework for liquid drops on soft substrates. This will allow computing the shape of drop and soft solid, and in particular establish the laws for the contact angles of drops on soft solids. This framework will subsequently be used to consider interactions between two neighbouring drops on a soft solid. To make progress on these macroscopic aspects, we will not focus on the microscopic details regarding the origin of the capillary forces. As such, we will consider the problem with $f_t = 0$ and $f_n = \gamma \sin \theta$.

Specifically, this thesis is organized as follows. In chapter 2 the general formalism used in this report will be set up: It starts by deriving the equilibrium conditions for both the soft solid and the liquid, through energy minimization. In chapter 3 we will solve the equations explicitly, providing us the shape of both the solid and liquid from which we will derive the contact angle a drop makes on a soft solid. It will also discuss different techniques to solve these equations, combining both theoretical and numerical techniques. In chapter 4 we will extent our model by introducing a second drop, using the same theoretical framework as in the previous chapters. Here we will reveal the nature of drop-drop interactions by using numerics and asymptotic analysis. Chapter 5 will reflect on the content of this thesis, and give suggestions for future research.

Chapter 2

Formalism

In this chapter we review the basic ingredients of elasticity and how elastic deformations arise due to capillary interactions. We first review some relevant elasticity theory in section 2.1 and discuss how this theory is used in our problem of a liquid drop on a soft solid. Section 2.2 will derive in detail through variational calculus what are the governing equations for elastic deformations arising due to capillary interactions. Subsequently, we will discuss in section 2.3 how we solve these governing equations describing the problem.

2.1 Elasticity and capillary tractions

When applying a force to an elastic body, the body tends to deform. In the specific case where these deformations originate from forces applied to its surface, rather than body forces, the stress tensor, $\bar{\sigma}$, satisfies [29]

$$\vec{\nabla} \cdot \bar{\sigma} = 0. \quad (2.1)$$

The constitutive equation relating stress to strain, e , for an isotropic elastic material, reads [29]

$$\bar{e}_{ij} = \frac{1}{E} [(1 + \nu)\bar{\sigma}_{ij} - \nu\sigma_{kk}\delta_{ij}], \quad (2.2)$$

where E is Young's modulus, ν Poisson's ratio and δ_{ij} the Kronecker delta function. Eq. (2.2) is also known as Hooke's law and assumes the experienced strains are small, such that it is only concerned with the linear elastic regime. We will solve the elastic problem, Eqs. (2.1) and (2.2),

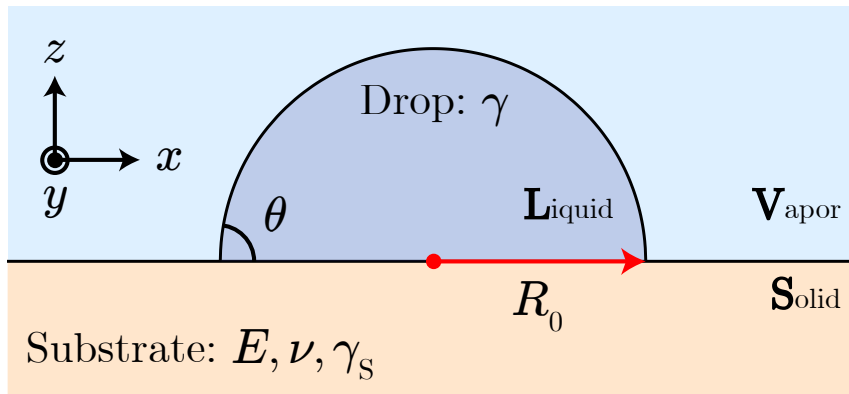


Figure 2.1: Schematic representation of a sessile drop on a substrate, having a solid surface tension γ_S . We chose the elastic modulus (E), and the Poisson ratio (ν), as relevant parameters to describe the elastic problem, but similarly the problem could have been equally defined in terms of, for example, the shear (G) and bulk modulus (K). Furthermore, the substrate is partially wetting, such that the liquid assumes the shape of a spherical cap having contact angle θ and contact radius R_0 .

using a Green’s function approach [30], which will be thoroughly addressed below. We will focus on 2-D drops, because derivations for axisymmetric drops will be very similar to the 2-D case. Moreover, in this thesis we will mainly focus on 2-D drops, but we will use and mention results for axisymmetric drops later on in chapter 3.

For our analysis in this chapter, consider a sessile drop on a soft solid as illustrated in Fig. 2.1. The soft solid is taken to be a semi-infinite elastic half-space, having elastic modulus E , Poisson ratio ν and solid surface tension γ_S . The sessile drop has surface tension γ , contact radius R_0 and contact angle θ . In this case, it is the drop which exerts a surface force on the solid surface under the action of capillary forces, thereby deforming the soft solid to a certain extent. When dealing with this problem, we will only consider capillary and elastic forces, not gravitational forces. Ignoring gravitational forces is justified as long as the typical drop radius R_0 is smaller than the capillary length $\lambda_c = \sqrt{\gamma/\rho g}$, that is, $R_0 < \lambda_c$. In this definition, ρ and g are the density of the liquid and the gravitational acceleration respectively. Moreover, we will assume for simplicity that the substrate is much thicker than R_0 for two reasons: First, this condition ensures that the problem does no longer depend on finite-thickness effects of the substrate [31] and secondly it allows us to adopt the plain-strain assumption [30]. The latter assumption is usually justified in practical situations and simplifies the derivation of elastic kernels involved in elastic theory. We will solve for the surface tractions *normal* to the elastic surface, by coupling the action of capillary forces to continuum elastic theory, similar to the work discussed in the previous section [12, 13, 14]. Under the assumption of an incompressible $\nu = 1/2$, tangential and normal displacements are decoupled, such that normal tractions can cause only normal deformations [13]. In our models, we will make one additional assumption regarding the elastic theory, being that all deformations occur in the solid’s elastic *linear* regime such that linear elastic theory [Eq. (2.2)] applies. For this assumption to be valid, the elastic strains have to be small which can be ensured by limiting γ/γ_S to a value of approximately 0.3 or smaller [30]. In addition, the small elastic strains also justify the small slope approximation we will adopt for the elastic surface ($h' \ll 1$), thereby allowing us to utilize a *linearized* expression of the local curvature at the solid surface.

Regarding the wetting properties of the soft solid, we will assume the interfacial energy’s of the solid-vapor and solid-liquid phase are equal, i.e., $\gamma_S = \gamma_{SV} = \gamma_{LV}$. Consequently, the typical contact angle in the problem will vary around $\theta \approx \pi/2$ according to Young’s relation which holds on rigid substrates, $\cos \theta = (\gamma_{SV} - \gamma_{SL})/\gamma$.

Elastic Green’s Functions— In the problem described in this report, the drop exerts a force at the boundary of the semi-infinite elastic substrate under the action of capillary forces. Therefore, we are only concerned with the stress components σ_{zx} , σ_{zy} and σ_{zz} . We note that $\sigma_{zx} = 0$, since we do not consider tangential stresses and $\sigma_{zy} = 0$ because the problem is invariant in y direction. We will now proceed denoting $\sigma(x) \equiv \sigma_{zz}$: Imposing the exact shape of the stress distribution, $\sigma(x)$, provides the strains e . However, exact solutions for an arbitrary function $\sigma(x)$ may be hard to find. The general approach is therefore to first seek a solution to Eq. (2.1) for a Dirac delta forcing $\delta(x)$; its solution is called the Green’s function \mathcal{K} . Now, since Eq. (2.1) is linear we can utilize the superposition principle by writing $\sigma(x)$ as an infinite sum of point forces and adding up all the solutions, resulting in the following solution:

$$h(x) = \int_{-\infty}^{\infty} dx' \sigma(x') \mathcal{K}(x' - x). \quad (2.3)$$

Derivations of elastic Green’s functions for *normal* tractions can be found in textbooks [29, 30]. We will simply mention them below, and discuss how they apply to our system.

2-Dimensional Green’s Function— The Green’s function for a line force of intensity unity, distributed along the y -axis and acting in a direction normal to the surface is [30]:

$$\mathcal{K}(x) = \left[\frac{2(1 - \nu^2)}{\pi E} \right] \ln \left(\frac{x_0}{|x|} \right). \quad (2.4)$$

Here x_0 is some outer length scale. The deformed shape of the surface thus has a logarithmic response to the line force. Eq. (2.4) has two unphysical complications, namely (i) the deformation

has a logarithmic dependence, hence does not converge in the far-field, and (ii) the displacement at the origin is infinite due to the singularity in stress at that point. This suggests we need a cut-off at both the small and large scale. Even though complication (i) is a direct consequence of the two-dimensional elastic problem, this complication does not arise for the finite size drops we are dealing with, because it can be shown that for a drop at equilibrium $\int dx \sigma(x) = 0$. Any solution to $h(x)$ is therefore independent on the choice of x_0 and does automatically converge in the far-field. Complication (ii) is a direct consequence of the infinite stress at the origin, but it has been shown that the solid surface tension γ_S regularizes the strain divergence [12, 32], thereby making the origin's displacement finite.

Calculating the elastic deformation of the solid, $h(x)$, through a Green's function approach by Eq. (2.3) requires knowledge of the stress distribution $\sigma(x)$. Inspired by chapter 1, we can hypothesize a stress distribution for a drop based on a mechanical point of view. As argued, Fig. 1.2 illustrates how the vertical component of the liquid-vapor tension, $\gamma \sin \theta$, is pulling at both contact lines $x = \pm R_0$, and how the Laplace pressure is pushing on the substrate in the center of the drop, $|x| < R_0$. It is easily shown the magnitude of the Laplace pressure equals $\Delta p = \gamma \sin \theta / R_0$ [1]. By modelling surface tension as a line force and including the solid capillary pressure, $\gamma_S h''$, similar to previous work [12], we hypothesize that

$$\sigma_{nn}(x) = \underbrace{\gamma \sin \theta \delta(x + R_0)}_{\text{lifting force contact line}} + \underbrace{\gamma \sin \theta \delta(x - R_0)}_{\text{lifting force right contact line}} + \underbrace{\gamma \frac{\sin \theta}{R_0} \Theta(|x| - R_0)}_{\text{Laplace pressure}} + \underbrace{\gamma_S h''}_{\text{solid Laplace pressure}}. \quad (2.5)$$

where $\delta(x)$ and $\Theta(x)$ are the Dirac delta and HeavisideTheta function respectively. We have sketched the drop-on-solid stress in Fig. 2.3, that is, Eq. (2.5) with the solid Laplace pressure excluded. Even though Eq. (2.5) suggests a particular form for $\sigma(x)$ its validity remains to be shown, which will be properly addressed in the next section.

2.2 Mechanical equilibrium through variational calculus

A sessile drop on a rigid surface ($E = \infty$) will take the equilibrium shape of a spherical cap, having a contact angle equal to Young's angle. The reason why it does so, is that the Helmholtz free energy

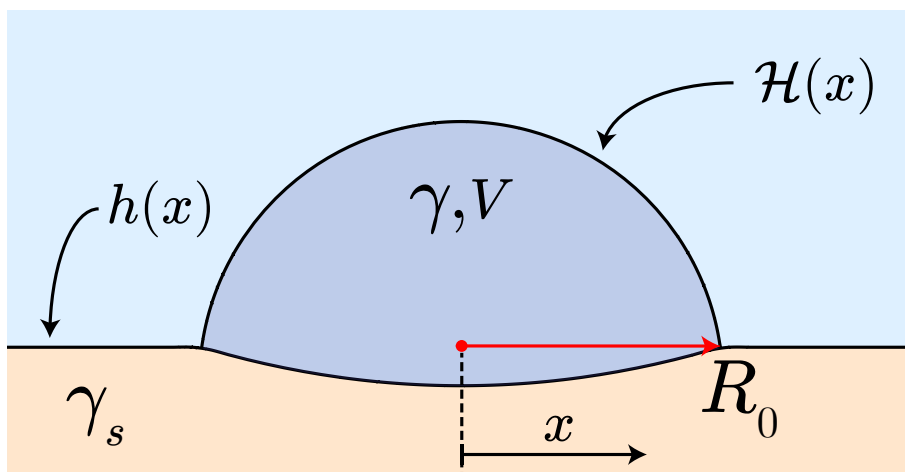


Figure 2.2: Definitions used for energy minimization. The liquid and solid surface are assigned the arbitrary functions $h(x)$ and $H(x)$, and carry a surface energy γ and γ_S , respectively. In addition, the solid has an energy contribution from elastic energy in the bulk. Energy is minimized under the constraint of a constant drop volume V , and a contact line located at $x = R_0$. In our definition for $h(x)$, $h = 0$ corresponds to a flat, undisturbed surface.

F is minimal for this particular configuration. Formally, this can be shown from a thermodynamic point of view, by minimizing the interfacial energies of the solid-vapor (SV), solid-liquid (SL) and liquid-vapor (LV) interfaces under a constant volume constraint. However when the substrate is no longer rigid, but elastic, one must in addition consider the energetic contributions of elastic deformations, leading to a departure from Young's law.

In this section we will formally derive what the equilibrium conditions are when taking into account the elastic and interfacial energies contributions of the substrate. In order to find the equilibrium configuration we minimize the total energy subject to its corresponding constraints, using a Lagrange multiplier method [33, 34]. Before we can proceed, we first have to identify the constraints and different energy contributions.

We start by writing down the total energy, which is a functional of the liquid surface $\mathcal{H}(x)$ and the solid surface $h(x)$ sketched in Fig. 2.3. The liquid surface contributes through its free surface energy F_γ . The solid surface has two contributions, namely: (i) Free surface energy of the solid F_S and (ii) the stored elastic energy F_{el} in the bulk. The total energy then equals

$$\boxed{F_{tot}[h(x), \mathcal{H}(x)] = F_{el}[h(x)] + F_S[h(x)] + F_\gamma[\mathcal{H}(x)]}. \quad (2.6)$$

The different energy contributions have the following functional form. First the liquid energy is found by integrating the surface area of the liquid,

$$F_\gamma[\mathcal{H}(x)] = \gamma \int_{-R_0}^{R_0} dx \left\{ \sqrt{1 + \mathcal{H}'^2(x)} \right\}. \quad (2.7)$$

Similarly, the surface area of the elastic solid, assuming small slopes, $h'(x) \ll 1$, is

$$\begin{aligned} F_S[h(x)] &= \frac{1}{2} \gamma_S \int_{-\infty}^{\infty} dx h'^2(x) \\ &= \frac{1}{2} \gamma_S \int_{-\infty}^{\infty} dq q^2 |\hat{h}(q)|^2. \end{aligned} \quad (2.8)$$

For convenience, we have directly written the interfacial energy of the solid as an integral carried out in Fourier space (see Appendix B). This will simplify our analysis later on. In order to avoid any convolutions involved when calculating the elastic energy, we will directly express the elastic energy in Fourier space as well [35]:

$$F_{el} = \frac{1}{2} \int_{-\infty}^{\infty} \frac{dq}{\sqrt{2\pi}} \frac{1}{\hat{\mathcal{K}}(q)} \hat{h}(q) \hat{h}(-q), \quad (2.9)$$

with $\hat{\mathcal{K}}(q)$ the Fourier transform (FT) of the elastic kernel defined in the previous section, Eq. (2.4). For the FT we use the unitary, angular wavenumber, q :

$$\mathcal{F}[f(x)] = \hat{f}(q) = \frac{1}{\sqrt{2\pi}} \int f(x) e^{iqx} dx, \quad \mathcal{F}^{-1}[\hat{f}(q)] = f(x) = \frac{1}{\sqrt{2\pi}} \int \hat{f}(q) e^{-iqx} dq.$$

Now that we have an expression for the total energy, the next step is to identify the appropriate constraints. Minimizing the total energy should be carried out under the conditions of:

1. Volume conservation. The drop volume V , should be conserved during energy minimization. Mathematically, we write the constraint F_1 as

$$F_1 = P \left\{ V - \int_{R_0}^{R_0} dx \left[\mathcal{H}(x) - h(x) \right] \right\}, \quad (2.10)$$

where P is a free Lagrange multiplier. The physical meaning of P will become apparent soon.

2. Three phase contact line at $x = \pm R_0$. At these points all different phases (SV , SL , LV) should meet. Symmetry conditions allow using identical Lagrange multipliers at both contact lines, such that the constraint F_2 becomes:

$$F_2 = \lambda \left\{ \mathcal{H}(R_0) - h(R_0) \right\} + \lambda \left\{ \mathcal{H}(-R_0) - h(-R_0) \right\}, \quad (2.11)$$

where λ is the second Lagrange multiplier.

We recombine the sum of constraints in the following way

$$\begin{aligned}
F_1 + F_2 &= P \left\{ V - \int_{R_0}^{R_0} dx \mathcal{H}(x) \right\} + \lambda_2 \left\{ \mathcal{H}(R_0) + \mathcal{H}(-R_0) \right\} \\
&\quad - \int_{-\infty}^{\infty} dx h(x) \left\{ \underbrace{\lambda \delta(x - R_0) + \lambda \delta(x + R_0) - P \Theta(R_0 - |x|)}_{\equiv f_{nn}(x)} \right\} \\
&= P \left\{ V - \int_{R_0}^{R_0} dx \mathcal{H}(x) \right\} + \lambda \left\{ \mathcal{H}(R_0) + \mathcal{H}(-R_0) \right\} - \int_{-\infty}^{\infty} dx h(x) f_{nn}(x),
\end{aligned}$$

with

$$f_{nn} = \lambda \delta(x - R_0) + \lambda \delta(x + R_0) - P \Theta(R_0 - |x|) \quad (2.12)$$

We thus find by using Parseval's theorem for the last term:

$$F_1 + F_2 = P \left\{ V - \int_{R_0}^{R_0} dx \mathcal{H}(x) \right\} + \lambda \left\{ \mathcal{H}(R_0) + \mathcal{H}(-R_0) \right\} - \int_{-\infty}^{\infty} dq \hat{f}_{nn}(q) h(-q). \quad (2.13)$$

Following the general procedure for minimizing through the use of Lagrange multipliers, we add the constraints to the total energy [33]:

$$\begin{aligned}
\tilde{F}_{tot}[h(x), \mathcal{H}(x)] &= F_{el}[\hat{h}(q)] + F_S[\hat{h}(q)] + F_\gamma[\mathcal{H}(x)] + F_1 + F_2 \\
&= \frac{1}{2} \int_{-\infty}^{\infty} \frac{dq}{\hat{\psi}(q)} \hat{h}(q) \hat{h}(-q) - \int_{-\infty}^{\infty} dq \hat{f}_{nn}(q) \hat{h}(-q) + PV \\
&\quad + \int_{-R_0}^{R_0} dx \left\{ \gamma \sqrt{1 + \mathcal{H}'^2(x)} - P \mathcal{H}(x) \right\} + \lambda \left\{ \mathcal{H}(R_0) + \mathcal{H}(-R_0) \right\},
\end{aligned} \quad (2.14)$$

with

$$\hat{\psi}^{-1}(q) = [\sqrt{2\pi} \hat{\mathcal{K}}(q)]^{-1} + \gamma_S q^2. \quad (2.15)$$

We are now in position to calculate the equilibrium conditions. These follow by carrying out the energy variation, through varying the functions $\mathcal{H}(x)$ and $h(x)$. The equilibrium conditions are found by setting $\delta \tilde{F}_{tot} = 0$, since any small variation in $\delta \mathcal{H}$ or δh should correspond to a zero change in energy when having minimum energy. Variation of the liquid interface $\mathcal{H}(x)$ and the elastic interface $h(x)$, give the equilibrium conditions for $\mathcal{H}(x)$ and $h(x)$, respectively.

2.2.1 Variation of the liquid interface: $\mathcal{H}(x)$

Variation of $\mathcal{H}(x)$ involves only terms that are a function of $\mathcal{H}(x)$. Hence, any variation in energy should be caused by the last two terms in Eq. (2.14). Carrying out the energy variation for $\delta \mathcal{H}$ yields,

$$\delta \tilde{F}_{tot} = \lambda \{ \delta \mathcal{H}(R_0) + \delta \mathcal{H}(-R_0) \} + \int_{-R_0}^{R_0} dx \left\{ \frac{\gamma \mathcal{H}'}{(1 + \mathcal{H}'^2)^{1/2}} \delta \mathcal{H}' - P \delta \mathcal{H} \right\} = 0.$$

Using integration by parts for the first term in the integral, we can write

$$\delta \tilde{F}_{tot} = \lambda \{ \delta \mathcal{H}(R_0) + \delta \mathcal{H}(-R_0) \} + \left[\frac{\gamma \mathcal{H}'}{(1 + \mathcal{H}'^2)^{1/2}} \delta \mathcal{H} \right]_{x=-R_0}^{x=R_0} - \int_{-R_0}^{R_0} dx \left\{ \frac{\gamma \mathcal{H}''}{(1 + \mathcal{H}'^2)^{3/2}} + P \right\} \delta \mathcal{H}(x).$$

The above result can be rewritten in its turn, by using

$$(i) \quad \mathcal{H}'(\pm R_0) / [1 + \mathcal{H}'^2(\pm R_0)]^{1/2} = \mp \sin \theta$$

2.2.2 Variation of the elastic interface: $h(x)$

Variation of $h(x)$ involves only the first two terms in Eq. (2.14), which both depend on $\hat{h}(q)$. Carrying out the energy variation for $\delta\hat{h}(q)$ yields,

$$\delta\tilde{F}_{tot} = \frac{1}{2} \int_{-\infty}^{\infty} dq \frac{1}{\hat{\psi}(q)} \left\{ \hat{h}(q)\delta\hat{h}(-q) + \hat{h}(-q)\delta\hat{h}(q) \right\} - \int_{-\infty}^{\infty} dq \hat{f}_{nn}(q)\delta\hat{h}(-q).$$

Using that $\hat{h}(q)\delta\hat{h}(-q) = \hat{h}(-q)\delta\hat{h}(q)$, since $h(x)$ should be real and even, we can simplify the result above such that it reads

$$\delta\tilde{F}_{tot} = \int_{-\infty}^{\infty} dq \left\{ \frac{\hat{h}(q)}{\hat{\psi}(q)} - \hat{f}_{nn} \right\} \delta\hat{h}(-q). \quad (2.18)$$

Setting $\delta F_{el} + \delta F_S = 0$ gives the equilibrium condition,

$$\boxed{\hat{h}(q) = \hat{\psi}(q)\hat{f}_{nn}(q)}. \quad (2.19)$$

Eq. (2.19) might be recast in the implicit form $\hat{h}(q) = \sqrt{2\pi}\hat{\mathcal{K}}(q) \left[\hat{f}_{nn}(q) - \gamma_S q^2 \hat{h}(q) \right] \equiv \sqrt{2\pi}\hat{\mathcal{K}}(q)\hat{\sigma}_{nn}(q)$. Taking the inverse Fourier transform (IFT) of $\hat{\sigma}_{nn}(q)$, we recognize $\sigma_{nn}(x)$ as being the total stress distribution, including the response of the solid surface tension:

$$\sigma_{nn}(x) = f_{nn}(x) + \gamma_S \frac{\partial^2 h}{\partial x^2} \quad (2.20)$$

The first term in this equation is the stress exerted by the drop on the solid surface, Eq. (2.17), and the second term is the drop-induced Laplace pressure of the solid surface [Fig. 1.4]. It is the latter term that suppresses the strain divergence at the contact lines [12, 32], as we will see in more detail in chapter 3. Moreover, since a product of functions in Fourier space corresponds to a convolution in normal space, we can equally write:

$$h(x) = \int_{-\infty}^{\infty} dx' \mathcal{K}(x' - x) \sigma_{nn}(x). \quad (2.21)$$

The obtained result in Eq. (2.21) is identical to the result in Eq. (2.3), which we had obtained by writing $\sigma_{nn}(x)$ as an infinite sum of point forces. At this point, however, energy minimization has shown the functional shape we can model the total stress distribution with, Eq. (2.20). In addition, note that Eq. (2.20) agrees with our hypothesized form of Eq. (2.5) which was obtained from a mechanical point of view.

Simplified expression for the total energy in the system— Using Eq. (2.19) it can be shown that the elastic (F_{el}) and free energy (F_S) contribution of the solid reorganize into a single term that is directly related to the drop's stress distribution, f_{nn} . Starting from Eq. (2.6) we know that the total energy in the system equals

$$F_{tot}[h(x), \mathcal{H}(x)] = F_{el}[h(x)] + F_S[h(x)] + F_\gamma[\mathcal{H}(x)]. \quad (2.22)$$

Expressions for each separate energy term are provided in Eqs. (2.7-2.9), such that F_{tot} yields

$$\begin{aligned} F_{tot} &= \frac{1}{2} \int_{-\infty}^{\infty} dq \left\{ \frac{\hat{h}(q)}{\sqrt{2\pi}\hat{\mathcal{K}}(q)} \hat{h}(-q) + \gamma_S q^2 \hat{h}(q)\hat{h}(-q) \right\} + \int_{-R_0}^{R_0} dx \left\{ \gamma \sqrt{1 + \mathcal{H}'^2(x)} \right\} \\ &= \frac{1}{2} \int_{-\infty}^{\infty} dq \underbrace{\frac{\hat{h}(q)}{\hat{\psi}(q)}}_{=f_{nn}(q)} \hat{h}(-q) + \int_{-R_0}^{R_0} dx \left\{ \gamma \sqrt{1 + \mathcal{H}'^2(x)} \right\} \end{aligned} \quad (2.23)$$

We can thus calculate the total energy as

$$\boxed{F_{tot} = \underbrace{\frac{1}{2} \int_{-\infty}^{\infty} dq f_{nn}(q)\hat{h}(-q)}_{F_{el}+F_S} + \underbrace{\int_{-R_0}^{R_0} dx \left\{ \gamma \sqrt{1 + \mathcal{H}'^2(x)} \right\}}_{F_\gamma}}. \quad (2.24)$$

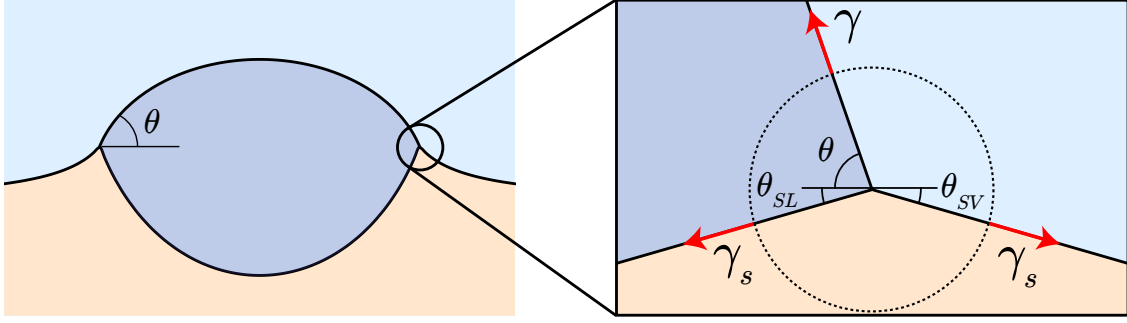


Figure 2.4: Schematics of the Neumann condition at the contact line. Stresses acting on the circular dashed control volume should balance in both horizontal and vertical direction. Vertical balance is automatically ensured by the elastic problem, but θ should be chosen such that there in addition is a horizontal balance of stresses, Eq.(2.25).

Importantly, the equation above shows that when calculating the total energy associated with the solid, one should only consider stresses exerted by the drop on the solid. Any contribution of the solid surface tension is indirectly captured through $h(x)$. We will use this equation in the next chapter in order to compare the relative energy contributions of the liquid and solid.

2.2.3 Closure of the problem through the contact angle θ

The approach of coupling the stress distribution of a drop to continuum elastic theory provided us the governing equations for the shapes of the solid and liquid interface. These equations, however, are not sufficient to close the complete problem, because they only state how the solid responds to the presence of a drop, and the other way around, but it leaves the contact angle θ undetermined. In particular, the contact angle sets itself such that it satisfies the horizontal Neumann condition [Fig. 2.4]:

$$\gamma \cos \theta + \gamma_S \cos \theta_{SL} = \gamma_S \cos \theta_{SV}. \quad (2.25)$$

Closure of the problem can thus be realized by coupling the horizontal Neumann condition to Eq. (2.21).

Formally, the horizontal Neumann condition can be shown by repeating the variational process for the contact line position R_0 , as was done for $\mathcal{H}(x)$. This variation, however, poses some difficulties because we have to integrate over the slope discontinuity at the contact line when solving the solid free energy by a FT. Even though we cannot perform this variation in this thesis yet, there is ample support horizontal Neumann holds at both contact lines [15].

2.3 Solving the equations

To summarize, we have obtained the following set of governing equations:

$h(x)$	$= \int_{-\infty}^{\infty} dx' \mathcal{K}(x' - x) \sigma_{nn}(x)$	(Solid shape)	
$\frac{\mathcal{H}''}{(1 + \mathcal{H}'^2)^{3/2}}$	$= P/\gamma$	(Liquid shape)	(2.26)
$\gamma \cos \theta + \gamma_S \cos \theta_{SL}$	$= \gamma_S \cos \theta_{SV}$	(Hor. Neumann)	

We can see from Eq. (2.26) that the elastic deformation of the solid, $h(x)$ depends on five system parameters: $h = h(x, E, R_0, \gamma, \gamma_S, \theta)$. The elastic modulus E enters through the kernel $\mathcal{K}(x)$ and the remaining four parameters through the stress distribution $\sigma(x)$. A proper non-dimensionalization

should reduce the number of dependent parameters. Both the dependent and independent variables h and x , have dimensions of length, thus a natural choice is to scale these variables by the droplet radius R_0 . We define

$$\tilde{x} = \frac{x}{R_0}; \quad \tilde{h} = \frac{h}{R_0}; \quad \frac{\partial^2}{\partial \tilde{x}^2} = R_0^2 \frac{\partial^2}{\partial x^2}.$$

Using these scaled variables, we can rewrite the total stress distribution Eq. (2.20) as

$$\sigma_{nn}(x) = \frac{\gamma}{R_0} \left[\sin \theta \tilde{f}_{nn} + \frac{\gamma_S}{\gamma} \frac{\partial^2 \tilde{h}}{\partial \tilde{x}^2} \right] \equiv \frac{\gamma}{R_0} \tilde{\sigma}_{nn}(\tilde{x}, \gamma/\gamma_S, \theta), \quad (2.27)$$

with

$$\tilde{f}_{nn} = \delta(\tilde{x} + 1) + \delta(\tilde{x} - 1) - \Theta(1 - |\tilde{x}|). \quad (2.28)$$

If we in addition rewrite the elastic kernel for $\nu = 1/2$, we obtain from Eq. (2.4) that $\mathcal{K} = 3/(2\pi E)\tilde{\mathcal{K}}$. Substituting these non-dimensional results in Eq. (2.21), we obtain

$$\tilde{h} \left(\tilde{x}, \frac{\gamma}{ER_0}, \frac{\gamma}{\gamma_S}, \theta \right) = \frac{3}{2\pi} \frac{\gamma}{ER_0} \int_{-\infty}^{\infty} d\tilde{x}' \tilde{\sigma}_{nn} \left(\tilde{x}', \frac{\gamma}{\gamma_S}, \theta \right) \tilde{\mathcal{K}}(\tilde{x}' - \tilde{x}). \quad (2.29)$$

We have now reduced the number of dependent parameters for h from five to three, and they are identified as the following parameters:

- (i) γ/ER_0
- (ii) γ/γ_S
- (iii) θ

Indeed, the ratio of elasto-capillary length γ/E to the drop radius R_0 manifests itself in the non-dimensionalized equations. For a given drop radius R_0 a large value of γ/ER_0 corresponds to a large γ/E , indicating the solid is soft. A small value of γ/ER_0 would correspond to a rigid solid using similar arguments. In subsequent analysis the parameter γ/ER_0 will return frequently, and we will therefore refer to it as the *softness* parameter. *In the upcoming chapters we will drop the tilde sign for dimensionless variables*, hence variables as h and x should then always be regarded as being normalized by the drop radius R_0 , unless the context states otherwise.

Moreover, recalling the equation for the liquid shape in Eq. (2.26) is simply a statement of $\mathcal{H}(x)$ having a constant curvature κ (see section 2.2.1), we know that the resulting solution must be a spherical cap with contact angle θ . In Appendix A its mathematical function is formally derived as

$$\mathcal{H}(x, \theta) = h_0 - \frac{R_0}{\tan \theta} + \sqrt{\left(\frac{R_0}{\sin \theta} \right)^2 - x^2}, \quad -R_0 \leq x \leq R_0, \quad 0 \leq \theta \leq \frac{\pi}{2}, \quad (2.30)$$

with h_0 the deformation of the solid at the contact line, that is $h_0 = h(x = R_0)$.

From Eqs. 2.29 and 2.30 it is clear the solutions for the solid and liquid shape are dependent on the adopted value for θ . Hence, the additional challenge is to find the correct contact angle θ , such that the horizontal Neumann condition Eq. (2.25) is satisfied. Apart from θ , the horizontal Neumann condition requires knowledge about the solid-vapor (θ_{SV}) and liquid-vapor (θ_{LV}) angles. The latter two angles, however, can only be known after solving the elastic problem [Eq. (2.29)] and hence knowing the solid shape, but its solution was already dependent on θ . Therefore it is *a priori* unclear whether one has obtained the correct solution, that is, the one satisfying horizontal Neumann. This suggests we need a feedback mechanism that resolves the elastic problem over and over, until a particular choice of θ results in the correct θ_{SL} and θ_{SV} , satisfying horizontal Neumann. Below we discuss how we set up this (iterative) feedback mechanism.

Iterative solving routine— The central starting point is the stress distribution $\sigma(x, \theta)$ which is convoluted with the elastic kernel $\mathcal{K}(x)$ in Eq. (2.29), yielding the solution for $h(x)$. Solving this equation (details are given in chapter 3) for an initial contact angle $\theta_1 = \theta_Y$ (Young’s angle), yields the surface deformation $h(x)$ for the particular choice of $\theta_1 = \theta_Y$. This solution, however, was found for an incorrect stress distribution $\sigma(x, \theta_Y)$ because the contact angle on a soft solid is in general not equal to Young’s angle, and hence does not obey horizontal Neumann at the contact line. Therefore we have to resolve the system with a new choice for θ , say θ_{n+1} , serving as input for $\sigma_{n+1}(x, \theta_{n+1})$ in the subsequent iteration $n + 1$. A numerical measurement of the θ_{SL} and θ_{SV} angle during iteration n , allows for an optimal new choice for θ_{n+1} . In particular, the best choice is $\cos \theta_{n+1} = (\gamma_S/\gamma) [\cos \theta_{SV,n} - \cos \theta_{SL,n}]$. Typically, we needed only $n = 3$ iterations to converge and satisfy horizontal Neumann with a numeric precision on the order of 10^{-12} . Once θ has converged, we directly know the exact equation for the liquid cap $\mathcal{H}(x, \theta)$ through Eq. (2.30).

Chapter 3

Single Sessile Drop

Using the formalism developed in chapter 2, we now solve the shape of the soft solid and a single liquid drop. In Section 3.1 we will analyze the solid shapes in detail and derive scaling laws for these solid shapes utilizing the rigid, $\gamma/ER_0 \ll 1$, and soft limit, $\gamma/ER_0 \gg 1$ as important guidelines. Section 3.2 will in detail focus on the geometry of the three phase contact line, revealing the contact angle a liquid drop makes on a soft solid exhibits two transitions when sweeping the parameter space of γ/ER_0 .

3.1 Surface deformations due drop presence

3.1.1 Two dimensional drop

The stress distribution on a substrate due to the presence of a sessile drop, was shown to equal

$$\sigma_{nn}(x) = \frac{\gamma}{R_0} \left[\sin \theta \left\{ \delta(x+1) + \delta(x-1) - \Theta(1-|x|) \right\} + \frac{\gamma_S}{\gamma} \frac{d^2 h}{dx^2} \right]. \quad (3.1)$$

We have seen both Dirac delta functions in Eq. (3.1) represent the drop-on-solid normal tractions, $\gamma \sin \theta$, at the contact lines, and the Heaviside-Theta function enters through the (liquid) Laplace pressure $\Delta p = \gamma \sin \theta / R_0$, pushing down on the solid. The last term in Eq. (3.1) serves as the solid capillary pressure, arising whenever the solid-liquid interface is curved. Physically, this means the drop presence induces a stress response of the solid, such that the equilibrium shape of both the solid and liquid are determined by the linear interplay of elasto-capillary interactions. Clearly, it is a direct consequence of including the solid surface tension γ_S in the problem, previously introduced in chapter 1.

In the previous chapter it was derived by coupling the stress distribution [Eq. (3.1)] to continuum elastic theory, that surface deformations $h(x)$ can be calculated through solving Eq. (2.29). Solving it poses some difficulties though, because $\sigma_{nn}(x)$ depends on the solution for $h(x)$ itself through the presence of h'' . Solving Eq. (2.29) therefore requires self-consistency, and in particular, since Eq. (2.29) involves both integrals (convolution) and derivatives of $h(x)$ it formally belongs to the type integro-differential equations. Following [12], a solution can be found using Fourier transforms, since (i) convolutions simplify greatly in Fourier-space, and (ii) derivatives of a function can be expressed in terms of the function itself, and both (i) and (ii) arise in Eq. (2.29). We shall now solve Eq. (2.29) by taking the FT¹, yielding

$$\begin{aligned} \hat{h}(q) &= \frac{3}{2\pi} \frac{\gamma}{ER_0} \sqrt{2\pi} \hat{\sigma}_{nn}(q) \hat{\mathcal{K}}(q) \\ &= \frac{3}{\sqrt{2\pi}} \frac{\gamma}{ER_0} \left(\sin \theta \hat{f}_{nn} - \frac{\gamma_S}{\gamma} q^2 \hat{h}(q) \right) \hat{\mathcal{K}}(q). \end{aligned} \quad (3.2)$$

¹For the Fourier transforms, we use the convention mentioned in chapter 2.

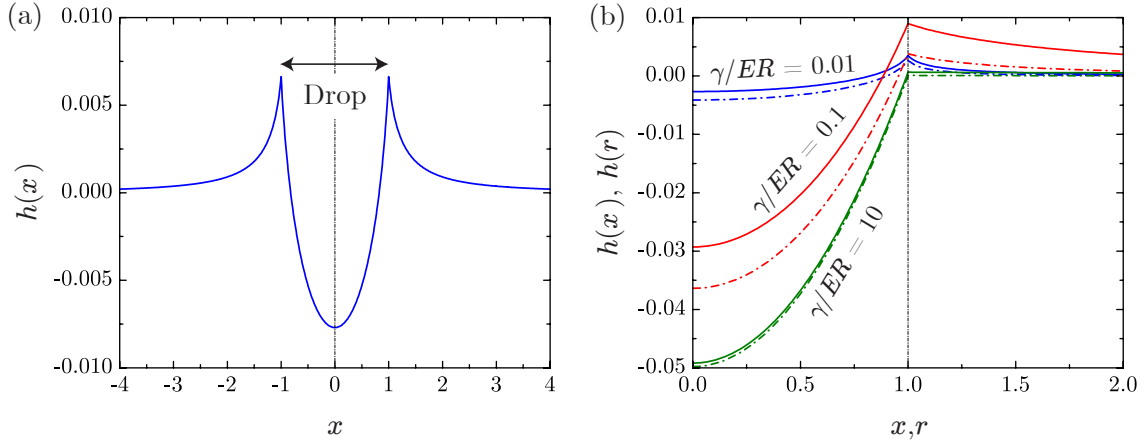


Figure 3.1: Calculated surface profiles for $\gamma/\gamma_S = 0.1$. (a) Surface profile for $\gamma/ER = 0.01$, obtained from 2-D theory. The drop is located at $|x| < 1$ (black arrow) and has its contact lines at $x = \pm 1$. (b) Surface profiles for three different values of the softness parameter γ/ER . Here we only show only one half of the symmetric surface profile, $\{x, r\} > 0$, with the contact line located at $\{x, r\} = 1$. Solid lines are results from 2-D theory, dash-dotted lines from 3-D theory. Note surface deformations are relatively small for $\gamma/ER = 0.01$, become larger for $\gamma/ER = 0.1$, and eventually reach a maximum dimple for $\gamma/ER = 10$. Surface deformations at the contact line ($\{x, r\} = 1$), however, appear to be non-monotonic with the softness parameter.

We now have obtained an implicit equation for $\hat{h}(q)$, which can be cast in explicit form for $\hat{h}(q)$,

$$\hat{h}(q) = \frac{\frac{3}{\sqrt{2\pi}} \frac{\gamma}{ER_0} \sin \theta \hat{f}_{nn}(q) \hat{\mathcal{K}}(q)}{1 + \frac{3}{\sqrt{2\pi}} \left(\frac{\gamma}{ER_0} \frac{\gamma_S}{\gamma} \right) q^2 \hat{\mathcal{K}}(q)}, \quad (3.3)$$

where the FT of $\hat{f}_{nn}(q)$ and $\hat{\mathcal{K}}(q)$ are calculated as

$$\hat{f}_{nn}(q) = \sqrt{\frac{2}{\pi}} \left(\cos q - \frac{\sin q}{q} \right) \quad \text{and} \quad \hat{\mathcal{K}}(q) = \sqrt{\frac{\pi}{2}} \frac{1}{|q|}. \quad (3.4)$$

Note the obtained result for $\hat{h}(q)$ is identical to what we would have obtained by directly employing relation (2.19).

The problem of finding the the elastic deformation of the solid, $h(x)$, is now refined to finding the IFT of Eq. (3.3). Unfortunately $\hat{h}(q)$ has a complex functional shape of products and fractions of functions, such that it does not allow for an exact solution for $h(x)$ through IFT. Instead, we use *Wolfram Mathematica 9* to carry out the IFT numerically. Fig. 3.1 displays a couple of numerically calculated surface profiles $h(x)$, for distinct values of the softness parameter, γ/ER_0 . In addition, Fig. 3.2 shows the complete solid and drop on different scales. Below we will give a brief physical discussion of the numerical results.

From chapter 1, it is expected that we should obtain a very similar shape of the solid $h(x)$, compared to those obtained in experiments or MD simulations (Fig. 1.2). Indeed, from Fig. 3.1(a) we clearly observe the solid is compressed directly under the drop, $x < 1$ and stretched around the contact line at $x = 1$. In particular, Fig. 3.1(b) shows how the solid deforms for different γ/ER_0 , thereby illustrating that for increasing γ/ER_0 the solid gets increasingly deformed directly under the drop. By contrast, increasing γ/ER_0 first leads to an increase of the deformation outside the drop and below the contact line, but subsequently decreases again when increasing γ/ER_0 even further. How can we explain the obtained profiles in Fig. 3.1(b)? Let us therefore first consider the deformation directly under the drop $x < 1$, and then the deformation at the contact line $x = 1$. We consider these two separately, because deformations under the drop are mainly set by the Laplace pressure, while deformations at the contact line are mainly set by the normal traction $\gamma \sin \theta$. Recalling the definition of the softness parameter, we know that for elasto-capillary lengths

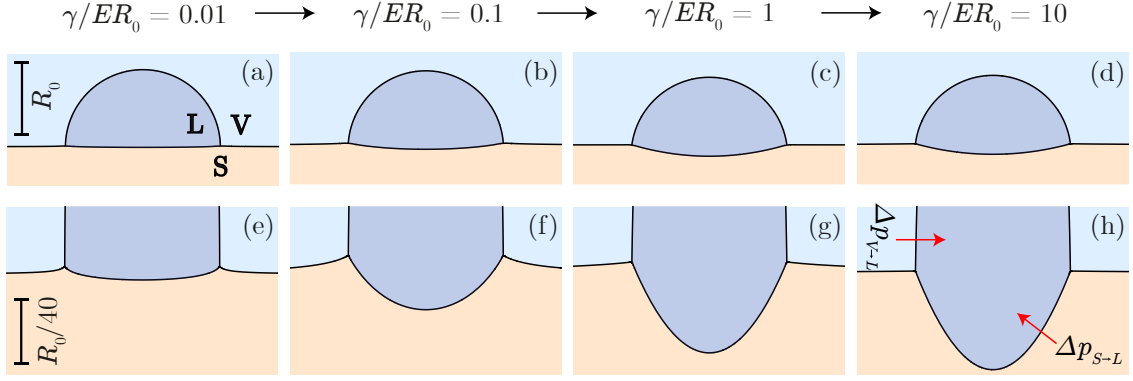


Figure 3.2: Output of the 2-D model, showing how the drop deforms the soft solid. Shapes of the solid and liquid are shown for different values of the softness parameter, γ/ER . Light orange, dark blue and light blue display the solid, liquid and vapor phase respectively. (a-d) As the solid becomes softer (increasing γ/ER) the drop "sinks" deeper in the substrate due increased compression of the solid. (e-h) Stretching the vertical scale shows the drop does not only compress the solid, but in addition it lifts the substrate at both contact lines, creating a so-called Neumann cusp. The image sequence shows the cusp initially grows in height for increasing softness, but by further increasing the softness the cusp subsequently relaxes again.

$\gamma/E \ll R_0$ we are dealing with a very rigid solid, that is, a high elastic modulus E . In the other limit, $\gamma/E \gg R_0$ we are dealing with a very soft solid, hence a low elastic modulus E . A simple physical picture regarding these solids is that they are essentially liquid-like, with an elastic modulus E to resist any shear deformation. Having this in mind, we are able to qualitatively explain the observed behaviour in Fig. 3.1(b).

Starting with the region directly underneath the drop, we note that the Laplace pressure Δp is barely able to deform rigid substrates (solid blue line). By increasing the softness of the substrate (solid red and green lines), however, the elasticity of the solid slowly vanishes and the Laplace pressure is less and less counteracted by elasticity. It therefore causes the "dimple" to grow, until, in the limit of vanishing elasticity, the solid is liquid-like and its final shape is given by a simple balance of capillary forces. In this case the liquid surface tension γ is balanced by the solid surface tension γ_S . The deformation at the contact line displays some more complex behaviour, however, since it appears to be non-monotonic with the softness of the solid. Clearly, the normal traction $\gamma \sin \theta$ at the contact line has difficulties deforming the solid for a high elastic modulus (solid blue line) similarly to the Laplace pressure, resulting in small deformations at the contact line. As the solid now becomes increasingly softer (solid red line), the solid allows for larger deformations, hence the effects of the normal traction become more pronounced. But for even softer solids (solid green line), elasticity is too weak to resist any normal force near the contact line, resulting in a decreasing deformation at the contact line. We will discuss this non-monotonic behaviour at the contact line and its implications in more detail in Section 3.1.3.

In the previous paragraph we have argued that in the limit of vanishing elasticity, $\gamma/E \gg R_0$, the solid cannot resist any shear and it behaves liquid-like. To illustrate this effect is indeed reflected by numerics, let us calculate the minimum $h(0)$ of the solid shape analytically from a balance of capillary forces only. This can be done by realizing that for a liquid-like solid elasticity is no longer important, such that the radius of curvature R_S of the soft solid should be a constant according to Laplace's equation $\Delta p = \gamma/R_S$, similarly to that of an ordinary liquid. Furthermore, by noting the pressure jump [Fig. 3.2] when crossing the curved vapor-liquid interface ($\Delta p_{V \rightarrow L}$), should equal the pressure jump when crossing the curved solid-liquid interface ($\Delta p_{S \rightarrow L}$), provides us an expression for the solid curvature, R_S :

$$\left. \begin{aligned} \Delta p_{V \rightarrow L} &= \gamma \sin \theta \\ \Delta p_{S \rightarrow L} &= \frac{\gamma_S}{R_s} \end{aligned} \right\} \rightarrow R_S = \frac{1}{\sin \theta} \frac{\gamma_S}{\gamma} \quad (3.5)$$

Using this curvature, it can readily be shown that $h(0) = -\gamma_S/(\gamma \sin \theta) + \sqrt{[\gamma_S/(\gamma \sin \theta)]^2 - 1}$. In

our case, we have $\gamma/\gamma_S = 0.1$ and $\theta \approx \pi/2 - \gamma/(2\gamma_S)$, such that we obtain: $h(0) \approx 0.05$. Note the perfect agreement with the green line in Fig. 3.1(b), reflecting that for $\gamma/E \gg R_0$ the soft solid indeed behaves liquid-like.

3.1.2 Axisymmetric drop

We also consider the surface deformations induced by an axisymmetric drop. By analogy to the 2-D drop [Eq. (2.27)], we find the stress distribution below an axisymmetric drop,

$$\begin{aligned}\sigma_{nn}(r) &= \frac{\gamma}{R_0} \left\{ \sin\theta f_{nn}(r) + \frac{\gamma_S}{\gamma} \nabla^2 h(r) \right\} \\ &= \frac{\gamma}{R_0} \left[\sin\theta \left\{ \delta(r-1) - 2\Theta(1-r) \right\} + \frac{\gamma_S}{\gamma} \frac{1}{r} \frac{\partial}{\partial r} \left(r \frac{\partial h}{\partial r} \right) \right].\end{aligned}\quad (3.6)$$

Here we have formulated the problem in polar coordinates (r, φ) , because the radial symmetry of the drop's contact line makes it natural to do so. Obviously, the stress distribution is independent on the azimuthal angle φ , because of the axisymmetry. In Eq. (3.6) a factor two enters the Laplace pressure term (Θ), since we have two identical principle curvatures in 3D. Accordingly, we calculate the surface deformation through the following integro-differential equation:

$$h(r) = \int_{-\infty}^{+\infty} \int_0^{2\pi} d\varphi dr' r' \sigma_{nn}(r') \mathcal{K}_{3D}(g(r', r, \varphi)), \quad (3.7)$$

where $g(r', r, \varphi)$ is some geometrical function and the elastic kernel equals [30]

$$\mathcal{K}_{3D}(r) = \left[\frac{(1-\nu^2)}{\pi E} \right] \frac{1}{r}. \quad (3.8)$$

In the previous section, we have solved the surface profile of a 2-D drop [Eq. (2.29)], in the framework of 1-D FTs for its advantages regarding convolutions and derivatives. For the same reasons it is advantageous to solve the deformation profile of an axisymmetric (3-D) drop in the framework of 2-D FTs. The first step in taking the 2-D FT of a function $F(r, \varphi)$ is switching from a Cartesian to polar coordinate system in the convention used for the FT, which could be done without loss of generality. To obtain the FT of the function $F(r, \varphi)$ one should then carry out the Fourier integrand with respect to r and φ . Now, if the function F happens to be radially symmetric, then $F(r, \varphi) = F(r)$ and the integration over ϕ may be carried out, without prior knowledge of the function $F(r)$. The two-dimensional FT $\hat{H}_0(s)$ and its inverse then simplify to [36]:

$$\hat{H}_0(s) = \int_0^\infty dr F(r) J_0(sr) r, \quad F(r) = \int_0^\infty ds \hat{H}_0(s) J_0(sr) s. \quad (3.9)$$

Here s is the wave-number, and J_0 is a zeroth order Bessel function of the first kind. Eq. (3.9) is known as a Hankel transform of the zeroth order. It is suitable only for two-dimensional FT of functions being radially symmetric and thus independent on φ , which is exactly what we have encountered regarding $\sigma_{nn}(r)$ and $\mathcal{K}_{3D}(r)$. The Hankel Transform has similar properties regarding convolutions and derivatives of functions [36], that will be useful for us:

$$\begin{aligned}H_0 \left\{ \int_0^\infty dr' \mathcal{K}(r'-r) F(r) \right\} (s) &= \mathcal{K}(s) F(s) \\ H_0 \left\{ \frac{1}{r} \frac{\partial}{\partial r} \left(r \frac{\partial F}{\partial r} \right) \right\} (s) &= -s^2 F(s).\end{aligned}\quad (3.10)$$

We are now in position to take the Hankel transform of Eq. (3.7). Doing so results in an implicit equation, similarly to the 2-D case in Eq. (3.2). Solving the resulting implicit equation for $\hat{h}(s)$, one obtains

$$\boxed{\hat{h}(s) = \frac{\frac{\gamma}{ER_0} \sin\theta \hat{f}_{nn}^S(s) \hat{\mathcal{K}}_{3D}(s)}{1 + \left(\frac{\gamma}{ER_0} \frac{\gamma_S}{\gamma} \right) s^2 \hat{\mathcal{K}}_{3D}(s)}}, \quad (3.11)$$

where the Hankel transforms of $\hat{f}_{nn}(s)$ and $\hat{\mathcal{K}}(s)$ are given by

$$H_0 \left\{ \tilde{f}_{nn}(r) \right\} (s) = J_0(s) - \frac{2J_1(s)}{s} \quad \text{and} \quad H_0 \left\{ \tilde{\mathcal{K}}_{3D}(r) \right\} (s) = \frac{2\pi}{s}, \quad (3.12)$$

with J_1 a first order Bessel function of the first kind.

Similar to the previous section, the problem is now refined to finding the inverse Hankel transform (IHT) of Eq. (3.11). Indeed, an exact IHT cannot be found, such that we again choose the numeric approach in order to find $h(r)$. As for the 2-D model, we have plotted a couple of surface profiles, $h(r)$, in Fig. 3.2. Note that we can directly compare 2-D and 3-D surface deformations, because $h(r)$ is invariant along the azimuthal direction.

Upon comparing 2-D and 3-D surface profiles, we observe from Fig. 3.1 that the profiles for $\gamma/ER_0 = 0.01$ (blue) and $\gamma/ER_0 = 10$ (green) are almost identical. Fig. 3.3 illustrates why 2-D and 3-D are almost identical in the case of $\gamma/ER_0 = 0.01$: If the elasto-capillary length becomes sufficiently small compared to the drop radius, that is, $\gamma/ER_0 \ll 1$, solid points in the periphery of the contact line do not feel the local curvature of the contact line anymore, but effectively experience a straight contact line instead. Since a 2-D drop has a simple straight contact line, the 2-D and 3-D approach give identical results in this limit. The agreement for the other set of profiles, $\gamma/ER_0 = 10$ (green) in Fig. 3.1, can simply be explained by regarding the solid as liquid-like. Writing a balance of capillary forces, similar to the previous section, Eq. (3.5), yields

$$\left. \begin{aligned} \Delta p_{V \rightarrow L} &= 2\gamma \sin \theta \\ \Delta p_{S \rightarrow L} &= 2 \frac{\gamma_S}{R_S} \end{aligned} \right\} \rightarrow R_S = \frac{1}{\sin \theta} \frac{\gamma_S}{\gamma}. \quad (3.13)$$

Here the factor two enters the equations, because we have two identical principal curvatures in 3-D. Balancing these pressures shows that the factor two cancels, leaving us with an identical result as for the 2-D case. We thus conclude that surface deformations caused by 2-D and 3-D drops converge to identical results in both the rigid $\gamma/ER_0 \ll 1$ and soft $\gamma/ER_0 \gg 1$ limit. For intermediate values of the softness parameter, however, finite curvature effects of the drop's contact line becomes apparent [Fig. 3.1(b)], even though it qualitatively exhibits the same behaviour.

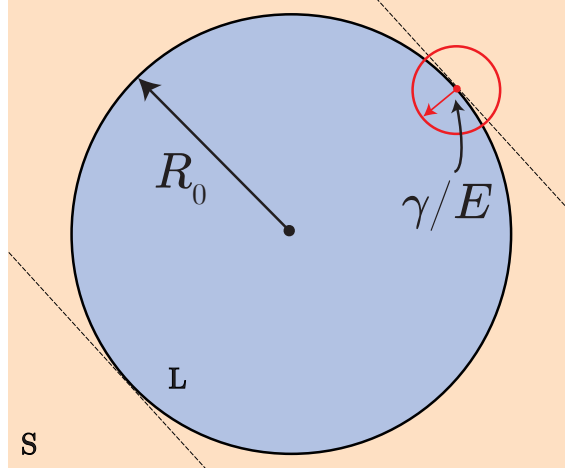


Figure 3.3: Topview of an axisymmetric sessile drop on a soft solid. Two circles are drawn, the large being the contact line of a drop of radius R_0 , the small (red) one has a radius equal to the elasto-capillary length γ/E . Dashed lines represent the contact lines of a 2-D drop. Since the typical range of deformation is γ/E , perturbations are felt approximately over a distance γ/E in the solid. If the elasto-capillary length becomes much smaller than the drop radius, $\gamma/ER_0 \ll 1$, the solid points within the red circle do no longer see the curvature of the drop's contact line, but see a straight contact line instead, as if it were a 2-D drop.

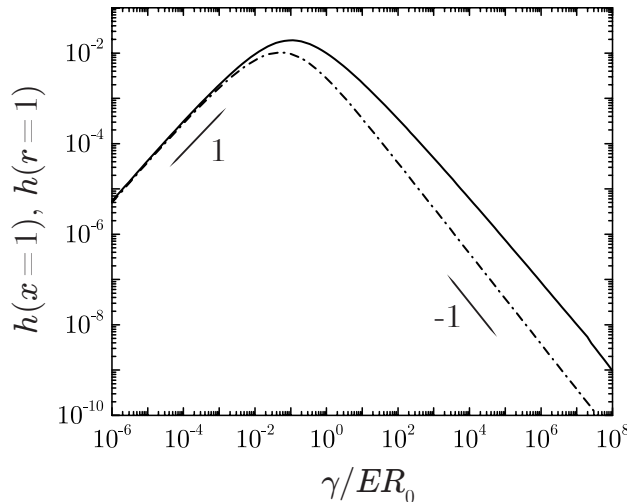


Figure 3.4: Surface deformations at the contact line as function of the softness parameter for $\gamma/\gamma_S = 0.1$: solid lines are results from 2-D theory, dash-dotted lines from 3-D theory. Deformations at the contact line are non-monotonic with the softness parameter and display a maximum deformation around $\gamma/ER \approx 0.1$, readily observed in Fig. 3.1. Using a log-log scale suggests that surface deformations are linear in γ/ER_0 (slope 1) in the rigid regime, $\gamma/ER_0 \ll 1$, and linear in ER_0/γ (slope -1) in the soft regime, $\gamma/ER_0 \gg 1$.

3.1.3 Asymptotics

As described Section 3.1 the deformation at the contact line displays non-monotonic behaviour when making the transition from the rigid to soft limit: It first increases and then decreases again, which we now have plotted in Fig 3.4, showing $h(x = 1)$ as a function of γ/ER_0 . The goal of this section is to derive the scaling laws describing the essential features of the deformations for 2-D and 3-D drops, inspired by the non-monotonic behaviour in Fig 3.4.

A closer inspection of Fig 3.4 suggests that deformations in the rigid limit are linear in γ/ER_0 . Similarly, we can argue that deformations in the soft limit appear to be linear in $(\gamma/ER_0)^{-1} = ER_0/\gamma$. These observations remain to be validated however, and one could therefore try to collapse surface profiles in the rigid and soft limit by proper scaling arguments. A collapse of surface profiles would then suggest we indeed have found the essential features of the deformations.

2-D similarity form— In Fig. 3.5(a,b) we have plotted 3 different surface profiles $h(x)$ on a log-log scale for both (a) the rigid limit, and (b) the soft limit. While Fig. 3.4 provides us the near field, $x = 1$, the surface profiles in Fig. 3.5(a,b) also provide us information about the far-field, $x \gg 1$. These surface profiles suggest that the far-field has a x^{-2} dependency, which can be shown analytically by going back to Eq. (3.3). We therefore first note that we expect surface deformations to decay smoothly in the far-field, such that it is dominated by long wavelength, mathematically corresponding to wave numbers going to zero, $q \rightarrow 0$. Taking the limit of Eq. (3.3) for $q \rightarrow 0$ should then provide us the far-field dependency on x , which we will do now by first writing a series expansion of Eq. (3.3) around $q = 0$ and then letting $q \rightarrow 0$. Eq. (3.3) has the following series expansion around $q = 0$:

$$\hat{h}(q) = \frac{\frac{3}{\sqrt{2\pi}} \frac{\gamma}{ER_0} \sin \theta \left(-\frac{q^2}{3} \right) \left(\frac{1}{|q|} \right)}{1 + \frac{3}{\sqrt{2\pi}} \frac{\gamma_S}{ER_0} q^2 \left(\frac{1}{|q|} \right)}. \quad (3.14)$$

Now taking the limit of $q \rightarrow 0$ and subsequently calculate the IFT of the resulting expression, yields

$$h(x) = \left(\frac{1}{\pi} \frac{\gamma}{ER_0} \sin \theta \right) \frac{1}{x^2}. \quad (3.15)$$

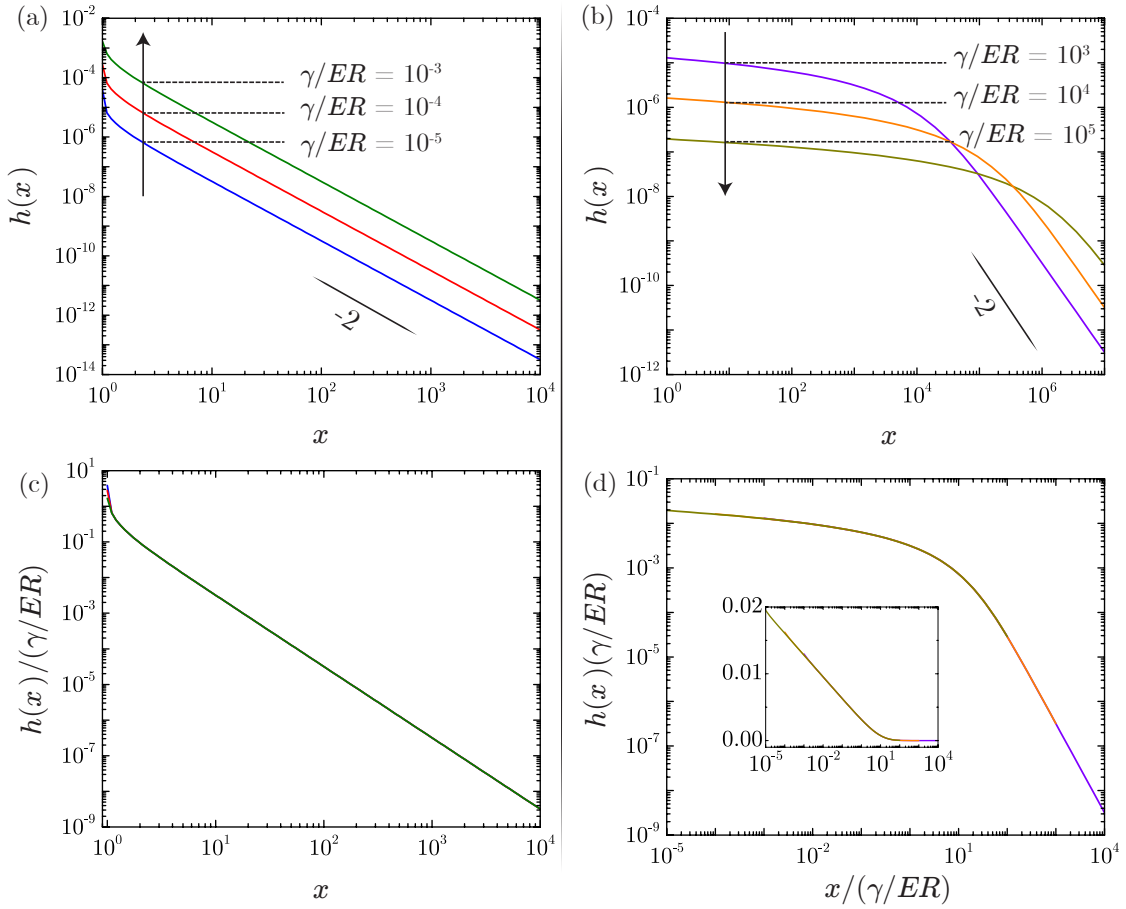


Figure 3.5: Surface profiles and a collapse of these numerical profiles in the rigid and soft regime. (a) Rigid regime, $\gamma/ER_0 \ll 1$. Three different surface profiles are shown, for which the deformations *increase* for increasing γ/ER_0 , indicated by the black arrow. Note the far-field ($x \gg 1$) decays as $\sim 1/x^2$. (b) Soft regime, $\gamma/ER_0 \gg 1$. Three different surface profiles are shown, for which the deformations *decrease* for increasing γ/ER_0 , again indicated by the black arrow. Similar to the rigid limit, the far-field in the soft limit decays as $\sim 1/x^2$. (c) Collapse of surface profiles obtained through scaling $h(x)$ by γ/ER_0 . (d) Collapse of surface profiles obtained through scaling $h(x)$ by ER_0/γ . If we in addition also rescale the x coordinate by γ/ER_0 we observe a collapse of profiles. The inset shows the near-field has a log-dependency, since plotting it on a log-linear scale results in a straight line.

Hence indeed, surface deformations in the far-field decays as $h(x) \sim x^{-2}$.

Moreover, Eq. (3.14) might be recast in the form

$$\hat{h}(q) = -\frac{1}{3} \sin \theta \frac{1}{\gamma_s/\gamma + \frac{1}{3} \sqrt{2\pi} \frac{ER}{\gamma|q|}}. \quad (3.16)$$

Introducing $Q = q\gamma/ER$, this gives

$$\hat{h}(q) = -\frac{1}{3} \sin \theta \frac{1}{\gamma_s/\gamma + \frac{1}{3} \sqrt{2\pi} \frac{1}{|Q|}} = -\frac{1}{3} \sin \theta \hat{G}(Q). \quad (3.17)$$

where $\hat{G}(Q)$ is the similarity solution of the far-field. The far-field expression $h(x)$ is then obtained by the IFT

$$\begin{aligned}
h(x) &= -\frac{1}{3} \sin \theta \frac{1}{\sqrt{2\pi}} \int dq \widehat{G}(Q) e^{-iqx} \\
&= -\frac{1}{3} \sin \theta \frac{ER}{\gamma} \frac{1}{\sqrt{2\pi}} \int dQ \widehat{G}(Q) e^{-iQxRE/\gamma} \\
&= -\frac{1}{3} \sin \theta \frac{ER}{\gamma} G\left(\frac{x}{\gamma/(ER)}\right). \tag{3.18}
\end{aligned}$$

We thus expect a collapse of the far-field profiles when plotting $h(x)\gamma/ER$ versus $x/(\gamma/ER)$, which is indeed confirmed in Fig. 3.5(d). In the stiff limit we do not need to rescale the x coordinate, because per definition $Q \ll 1$ in this limit. Indeed, we observe a collapse in Fig. 3.5(c) by only scaling $h(x)$.

The small- x behavior of the far-field displacement ultimately has to be comparable to the elastic deformation at the contact line. Formally, this should come from a matching procedure, where (3.18) should be matched to the large-scale asymptotics of the inner solution valid in the vicinity of the drop. Here we proceed by estimating the scaling of $h(x=1)$ with γ/ER , simply by evaluating (3.18) at $x=1$. This gives

$$h(1) \sim \frac{ER}{\gamma} G\left(\frac{ER}{\gamma}\right). \tag{3.19}$$

Since we consider the soft limit where $ER/\gamma \ll 1$, the scaling is readily inferred from $G(\epsilon)$ for small ϵ . It appears from Fig. 3.5(d) that $\lim_{\epsilon \rightarrow 0} G(\epsilon)$ approaches a constant value, from which it would follow that $h(1) \sim (\gamma/ER)^{-1}$, as is approximately observed in Fig. 3.4. However, the Fourier inversion of \widehat{G} at $\epsilon=0$ diverges, since the integral diverges at large Q , hence

$$\int_{-\infty}^{\infty} dQ \widehat{G}(Q) \rightarrow \infty. \tag{3.20}$$

Our numerical solution suggests a logarithmic divergence, such that we expect logarithmic corrections to the -1 scaling in Fig. 3.4. This is supported by the inset in Fig. 3.5(d), since the near-field on a log-linear scale results in a straight line. Hence, Eq. (3.19) has logarithmic corrections,

$$h(1) \sim \frac{ER_0}{\gamma} \log \frac{\gamma}{ER_0} \tag{3.21}$$

3-D similarity form— We can now proceed in a similar manner for the far-field solution of the 3D axisymmetric problem. Writing a series expansion of Eq. (3.11) around $s=0$, and taking the limit $s \rightarrow 0$, provides us the far-field expression

$$h(r) = \left(-\frac{\pi}{8} \frac{\gamma}{ER_0} \sin \theta\right) \frac{1}{r^3}, \tag{3.22}$$

showing the far-field for axisymmetric drops decays as $h(r) \sim 1/r^3$. In particular, the series expansion of Eq. (3.11) can be written as,

$$\hat{h}(s) = -\frac{1}{8} \sin \theta \frac{1}{\gamma s/\gamma + \frac{1}{2\pi S}} = -\frac{1}{8} \sin \theta \widehat{G}(S), \tag{3.23}$$

where we defined $S = s\gamma/ER$. This gives

$$\begin{aligned}
h(r) &= -\frac{1}{8} \sin \theta \int dq \widehat{G}(S) J_0(sr) s \\
&= -\frac{1}{8} \sin \theta \left(\frac{ER}{\gamma}\right)^2 \int dS \widehat{G}(S) J_0(SrRE/\gamma) S \\
&= -\frac{1}{8} \sin \theta \left(\frac{ER}{\gamma}\right)^2 G\left(\frac{r}{\gamma/(ER)}\right). \tag{3.24}
\end{aligned}$$

where $\widehat{G}(S)$ is the similarity solution of the far-field. Using *Wolfram Mathematica*, the inverse Hankel transform could be evaluated and expanded for small arguments as $G(\epsilon) \sim 1/\epsilon$. Once more setting $r = 1$ in (3.24), we thus obtain

$$h(1) \sim (\gamma/ER)^{-1}, \quad (3.25)$$

and explains the behavior in the soft limit in Fig. 3.4.

3.2 From rigid to soft: Two transitions of the contact angles

The goal of this section is to identify the contact angle θ a liquid drop makes on a soft solid. We will show that the contact angle exhibits two transitions when increasing the softness parameter γ/ER_0 , and subsequently calculate θ as a function of the softness parameter.

3.2.1 Is surface tension perfectly localized?

The geometry of the three phase contact line is governed by two classical laws describing the macroscopic contact angles, sketched in Fig. 3.6. In the limit of a perfectly rigid substrate, $E = \infty$, the contact angle is governed by Young's law. In the other limit, $E = 0$, Neumann's law for a drop floating on a liquid substrate holds. One would therefore expect that the macroscopic contact angle makes a transition from Young's law to Neumann's law somewhere in the limit of vanishing elasticity $E \rightarrow 0$.

Recently, Marchand et al. [15] found that by using density functional theory (DFT), the transition from Young-to-Neumann takes place when the elasto-capillary length γ/E [Eq. (1.1)] reaches the order of molecular interactions, a . Hence, for $\gamma/Ea \ll 1$ the contact angle equals Young's angle, but for $\gamma/Ea \gg 1$ one recovers Neumann's angle. Clearly, the molecular scale a plays a crucial role for this transition in contact angle, but the scale a is absent in the framework that we have used up to now. This framework implicitly assumes the contact line force can be represented by a line-force of zero width, hence giving rise to δ -functions in Eq. (3.1). However, there is ample support surface tension is spread out on the molecular scale and not perfectly localized [11, 19]. Fig. 3.7(c) demonstrates by MD simulations that surface tension is indeed spread out: it varies around the liquid-vapor interface by a couple of molecular diameters d , but it has an integrated area equal to γ . While modelling the normal traction f_{nn} by a Dirac delta function assumes that $a = 0$, in contrast, MD simulations suggest that $a \neq 0$.

Ignoring this finite size effect on scale a will restrain the transition from Young's law to Neumann's law according to Marchand's work, and result in an incorrect physical picture: The contact angle a liquid drop makes on a solid is then always governed by Neumann's law, while *a priori* it is clear that on a perfectly rigid substrate the contact angle should satisfy Young's law. The origin of this problem lies in the elastic theory: While Young's modulus E (dimension N/m^2) is the typical pressure scale a solid can resist before deforming significantly, the typical pressure scale of the capillary traction is γ/a . Comparing these two pressure scales for a finite E shows that for a line force $a \rightarrow 0$, one always has $\gamma/a \gg E$, such that the solid is "soft" (*i.e.* always deforms) with respect to this contact line force. Assuming γ is spread out on scale a ($a \neq 0$), on the other

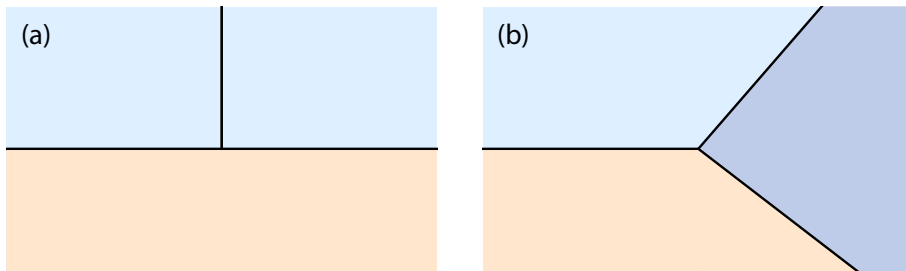


Figure 3.6: Contact angle geometry for (a) Young's law on a perfectly rigid substrate, and (b) Neumann's law for a drop floating on a liquid substrate.

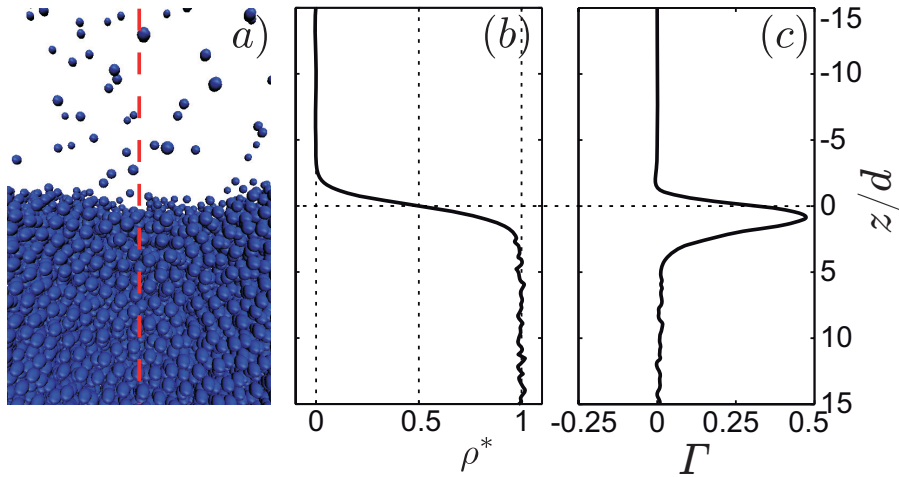


Figure 3.7: A liquid-vapor interface. The vertical z -axis has units of the molecular scale d . (a) Snapshot of the MD simulation for a liquid-vapor interface. (b) Time-averaged density profile ρ^* across the interface, normalized by the liquid density. (c) Stress exerted by the left part on the right part of the system, showing that surface tension is spread out over a couple molecular diameters. Image adapted from [11].

hand, results in $\gamma/a \ll E$, such that the solid is always "rigid" (*i.e.* never deforms if E is large enough) with respect to the contact line force. We therefore conclude that modelling the capillary traction as a perfect line force *always* results in a cusp shaped interface at the contact line, but modelling it as force spread out on the molecular scale however, results in a flat interface. These two different scenarios are sketched in Fig. 3.8.

From Fig. 3.8 one can easily imagine that the microscopic contact angle the drop makes, microscopic being on the scale a , are totally different in Figs. 3.8(a) and (b). Obviously, the situation sketched in (b) is the physically correct one, because it reflects Young's law [15] by taking into account the molecular size a . Importantly, we thus have to include the microscopic parameter a in our macroscopic model in order to find the correct qualitative behaviour of θ . We will account for the surface tension being spread on the molecular scale by modelling the surface tension as a very narrow Gaussian, $\Gamma(x)$, similar to the shape obtained in MD simulations, Fig. 3.7. In particular we will use a *normalized* Gaussian,

$$\Gamma(x) = \gamma \frac{1}{a\sqrt{2\pi}} e^{-\frac{1}{2}\left(\frac{x}{a}\right)^2}, \quad (3.26)$$

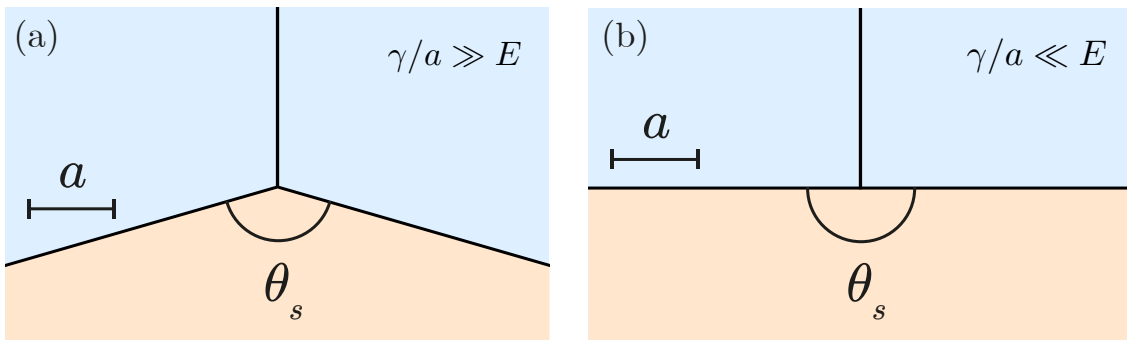


Figure 3.8: Surface shapes in the limit of $\gamma/a \gg E$ and $\gamma/a \ll E$ on typical scale a . (a) Modelling surface tension as a perfect line force, $a = 0$. The infinite stress at the contact line deforms the solid such that a cusp is formed, $\theta_s \neq \pi$. (b) Modelling surface tension as a force spread out on the molecular scale a . In this case the capillary traction $\Gamma(x)$ is too weak compared to elasticity for any deformation to occur, such that the interface is flat, $\theta_s = \pi$.

where we have checked that $\int_{-\infty}^{\infty} \Gamma(x) = \gamma$. Indeed, this is a classical representation of the δ -function in the limit $a \rightarrow 0$ [37].

Replacing both Dirac delta functions $\delta(x \pm 1)$ in the stress distribution [Eq. (3.1)] by two narrow Gaussian's $\Gamma(x \pm 1)$, introduces the microscopic parameter a in our model. We now have a macroscopic model that also accounts for the spread out effect of surface tension on a microscopic scale. Moreover, we will use this updated model to numerically investigate how both the micro and macroscopic contact angle θ is characterized as a function of the softness parameter γ/ER_0 in the next section.

3.2.2 Geometry of the contact line as function of softness parameter

By solving the governing equation, Eq. (2.29), we can sweep through the entire parameter regime of γ/ER_0 and measure the geometry of the contact line for each value of γ/ER_0 . In particular, we determine the geometry of the contact line by measuring θ_S , θ_{LV} and θ_{SL} numerically, the angles previously being defined in Fig. 2.3. From these angles, we have plotted the quantities, (i) $\theta_{SL} + \theta_{SV}$ and (ii) $\theta_{SL} - \theta_{SV}$ in Fig. 3.9. We have chosen to plot these particular quantities, because each of them reflects a transition the contact angle θ makes:

- (i) $\theta_{SL} + \theta_{SV} = \pi - \theta_S$: First transition controlled by the scale of molecular interactions a . One witnesses a transition of contact line geometry from Young's to Neumann's law [15], when γ/E reaches the scale of molecular interactions a . At this point the solid becomes soft enough, is stretched, and develops a cusp, often referred to as a "Neumann-cusp" visible on the *microscopic* scale, but not on the *macroscopic* scale. How the geometry of the contact line is altered by this transition has been sketched in the top and bottom part of Fig. 3.9, for the micro and macroscopic point of view respectively.
- (ii) $\theta_{SL} - \theta_{SV} = 2\varepsilon$: Second transition controlled by the drop size R_0 . Here a solid body rotation of the three interfaces over an angle ε takes place when γ/E reaches the scale of the drop R_0 . During this transition, the actual microscopic contact angles itself do not change, they are only rotated over an angle ε . As such, the solid angle θ_S remains unaltered, which can be seen from the $\pi - \theta_S$ curve. In Fig. 3.9 we have again illustrated how the geometry of the contact line is altered by this second transition, both on the micro and macroscopic scale. Note that this transition, in contrast to the first transition is visible on the macroscopic scale. In fact, one could recognize the sketched macroscopic picture as a liquid lens floating on a liquid substrate.

An important consequence regarding these transitions is that the contact angles, *i.e.* the true wetting angles, are selected on the microscopic scale. In the highly strained region of a few molecular sizes around the contact line a Neumann-like cusp develops when γ/E reaches the molecular scale a which selects the contact angles. Any further increase of γ/E solely introduces a rotation of the system, but does not change the actual contact angles anymore.

We have also plotted transition (ii) for axisymmetric drops in Fig. 3.9 for sake of completeness, showing the same qualitative transition, indicated by the dash-dotted line. We have excluded transition (i) for axisymmetric drops, because we expect 2-D and 3-D drops to behave identically if $\gamma/ER_0 \ll 1$, based on argumentation in section 3.1.2.

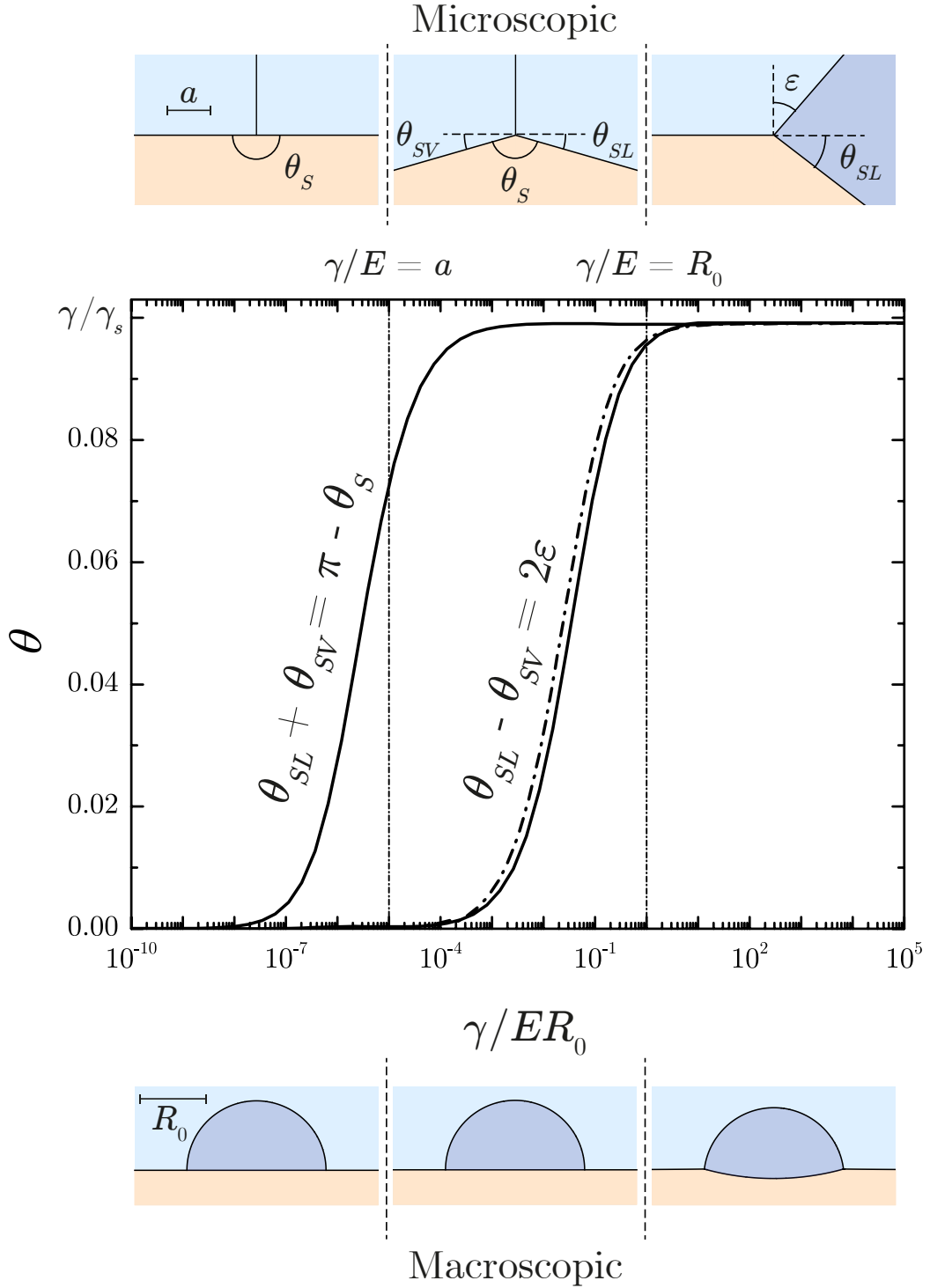


Figure 3.9: Predictions of the model derived in chapter 2 for $\gamma/\gamma_s = 0.1$ (solid lines: 2-D, dot-dashed lines: 3-D), modified to take into account the finite size a over-which forces are exerted at the contact line. We have plotted the angular deviation of the solid angle, $\pi - \theta_s$ and rotation angle ϵ , with corresponding microscopic (scale a) and macroscopic (scale R_0) pictures of the drop. This shows that (i) the microscopic geometry of the contact line first develops a Neumann-like cusp when γ/E is of the order of microscopic scale a , (ii) the macroscopic angle of the drop is altered only when γ/E reaches the size of the drop R_0 . The ratio R_0/a was taken 10^5 . Since a is typically on the order of nano-meters, this would in practice correspond to a typical drop radius that is sub-millimeters.

While Fig. 3.9 illustrates there are two transitions by plotting the sum and difference of θ_{SV} and θ_{SL} , it does not directly reflect how these angles behave on their own. As such, we have plotted θ_{SV} and θ_{SL} separately below in Fig. 3.10. It provides us some additional information: During the first transition, the development of the Neumann-cusp, θ_{SV} and θ_{SL} angle increase equally at the cost of the decreasing solid-angle θ_S . For increasing γ/ER_0 the point is reached where these two curves start to deviate from one another, indicating the second transition sets in and rotation of interfaces takes place. In fact, because the solid angle remains unaltered during this transition [Fig. 3.9], the increase in θ_{SL} equals the decrease in θ_{SV} .

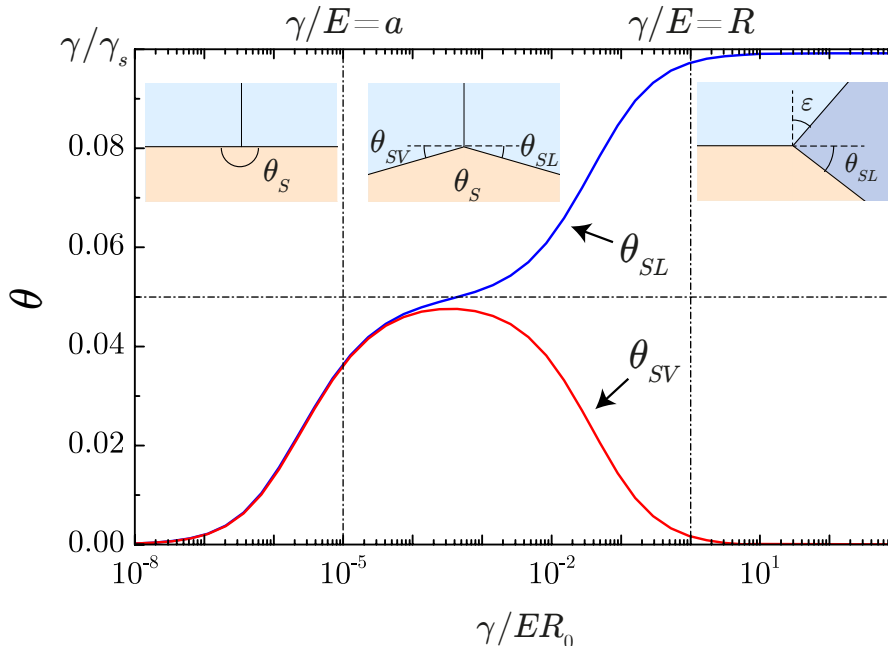


Figure 3.10: Numerical results for θ_{SV} and θ_{SL} as function of γ/ER_0 . Note that during the cusp formation around $\gamma/E = a$ the solid-vapor and solid-liquid angle are increasing equally, i.e., $\theta_{SV} = \theta_{SL}$. When γ/E reaches the drop size R_0 , the rotation of interfaces sets in, leading to an increase of θ_{SL} and decrease of θ_{SV} with respect to the horizontal.

3.3 Free energy as function of the softness parameter

Varying the softness parameter has provided us the micro and macroscopic contact angle a liquid drop makes on a soft solid. Varying the softness of the substrate can in addition also provide insight into energy changes associated with this varying softness. For a single drop on a soft solid, we have previously identified the following energy contributions: (i) Free surface energy of the solid F_S , (ii) the internal elastic energy F_{el} and (iii) the free surface energy of the liquid F_γ . The goal of this section is to calculate changes in each of these contributions as a function of the softness parameter γ/ER_0 , while using a drop on an infinitely rigid solid ($E = \infty$) as a reference case. When calculating energy changes it is important that we are looking at the same physical system, i.e., the same volume of liquid for all γ/ER_0 . As elastic deformations of the substrate will change the shape of the drop, there is no reason the distance between the contact lines R_0 is constant. We therefore scale the contact radius R_0 by a factor α to ensure volume conservation, where α should be determined numerically.

In Fig. 3.11 we have calculated the different energy contributions as a function of γ/ER_0 for both (a) $\gamma/\gamma_s = 0.1$ and (b) $\gamma/\gamma_s = 0.5$. Different contributions have been calculated using the equations stated below. For a detailed derivation of these equations we refer to appendix B, but importantly note that we calculate energies associated with the solid directly in Fourier space for efficiency.

$$\begin{aligned}
\frac{F_S}{\gamma R_0} &= \frac{1}{2} \left(\frac{\gamma_s}{\gamma} \right) \int dq q^2 |\hat{h}(q)|^2 \\
\frac{F_{el} + F_S}{\gamma R_0} &= \frac{3}{2\sqrt{2\pi}} \left(\frac{\gamma}{ER_0} \right) \int dq \hat{f}_{nn}(q) \hat{\sigma}(-q) \hat{K}(q) \\
\frac{F_\gamma}{\gamma R_0} &= \frac{2\alpha\theta}{\sin\theta} - \pi
\end{aligned} \tag{3.27}$$

From Fig. 3.11 we first observe that the qualitative behaviour for all energy contributions as a function of γ/ER_0 is the same for both $\gamma/\gamma_S = 0.1$ and $\gamma/\gamma_S = 0.5$. Secondly, the total energy (black lines) decreases when γ/ER_0 increases. The dominant mechanism for this total energy decrease is the capillary liquid energy (red line), decreasing more rapidly than the increasing energy terms associated with the solid (green and blue line). One can explain the increase in the solid capillary energy (green line) by the fact that more solid interface is created as the solid becomes softer, the maximum corresponding to a liquid lens floating on a liquid substrate. Interestingly, the elastic energy (blue curve) displays a maximum, which can be explained as follows. As the solid becomes increasingly softer, deformations increase and accordingly the elastic energy increases. However, if the solid becomes even softer, elasticity E vanishes such that elastic energy can no longer be stored in the elastic medium.

Because the total energy decreases for increasing γ/ER_0 (black lines in Fig. 3.11), we conclude drops preferably locate themselves at regions of low stiffness (high γ/ER_0). In other words, if a drop is placed on a substrate of variable stiffness $\gamma/ER_0(x)$, it experiences a driving force $f = -dF_{tot}/dx$ towards the region of lower stiffness. It should be realized that this driving force assumes that the drop radius is much smaller than the typical stiffness gradient, that is, $1/R_0 \ll \partial(\gamma/ER_0)/\partial x$, such that E might be regarded constant in the vicinity of the drop. Assuming this is the case, we can use our results in Fig. 3.11 to verify the explanation Style *et al* [23] gave for the observed durotaxis described in section 1.2. In their analysis they did not take into account the variation of elastic, neither the solid capillary energy as drops move over a substrate, thereby implicitly assuming the reduction of liquid capillary energy is dominant. While it is *a priori* not clear this would be the case, our numerical results in Fig. 3.11 have now shown that the reduction of liquid capillary energy is indeed dominant.

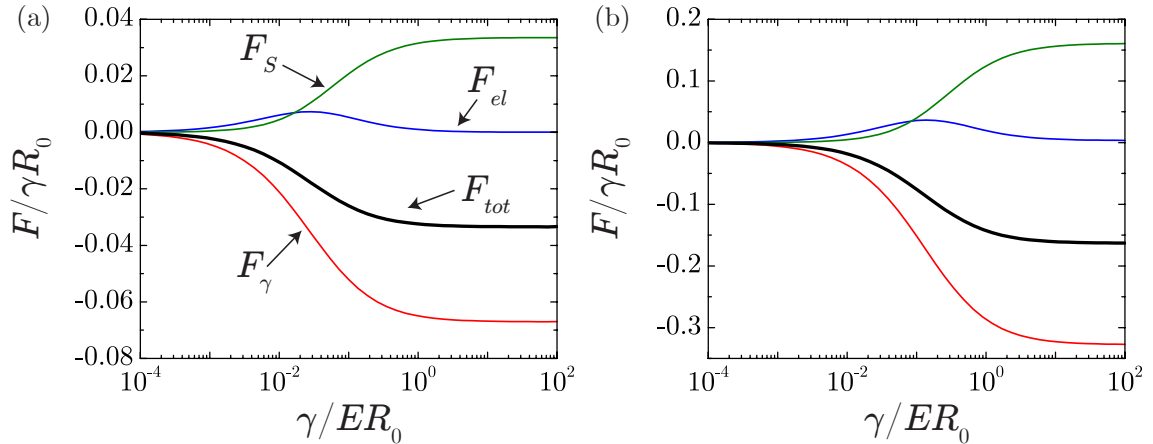


Figure 3.11: Changes in elastic energy F_{el} , capillary solid energy F_S , and capillary liquid energy F_γ as a function γ/ER_0 , where we have used a drop on a rigid substrate ($E = \infty$) as the reference case. (a) Energy changes for $\gamma/\gamma_S = 0.1$ and (b) $\gamma/\gamma_S = 0.5$.

Limiting energy F_S by a balance of capillary forces— In the limit of vanishing elasticity $E \rightarrow 0$, one should recover a perfect balance of capillary forces, that is a balance between the surface tensions γ_S and γ . In that case, we can calculate the limiting values of F_S exactly, derived below. In this derivation we will use the expression for the solid curvature R_S provided by Eq. (3.5).

$$\begin{aligned}
\lim_{\gamma/ER_0 \rightarrow \infty} E_S &= \frac{1}{2} \gamma_S R_0 \int_{-1}^1 dx \left| \frac{\partial h}{\partial x} \right|^2 \\
&= \frac{1}{2} \gamma_S R_0 \int_{-1}^1 dx (R_S^{-1} x)^2 \\
&= \frac{1}{3} \gamma_S R_0 R_S^{-2}
\end{aligned} \tag{3.28}$$

Hence

$$\frac{E_S}{\gamma R_0} = \frac{1}{3} \left(\frac{\gamma}{\gamma_S} \right) \sin^2 \theta \quad \text{for} \quad \gamma/ER_0 \rightarrow \infty \tag{3.29}$$

Upon substituting $\theta \approx \pi/2 - \gamma/(2\gamma_S)$ we find in the limit of $\gamma/ER_0 \rightarrow \infty$, that $E_S/(\gamma R_0) \approx 0.033$ for $\gamma/\gamma_S = 0.1$, while we find $E_S/(\gamma R_0) \approx 0.156$ for $\gamma/\gamma_S = 0.5$. Note these calculated values agree perfectly with the numeric results (green lines) shown in Fig. 3.11.

3.4 Summary

In this chapter we have solved the shape of the soft solid and a single liquid drop by coupling the action of capillary forces to elastic theory. Shapes were calculated for different values of the softness parameter γ/ER_0 , showing that for increasing γ/ER_0 the solid gets increasingly deformed directly under the drop [Figs. (3.1-3.2)]. The deformation at the contact line, however, was shown to display a maximum around $\gamma/ER_0 \approx 0.1$ [Fig. 3.1 and Fig. 3.4]. We have explained this maximum by arguing that deformations increase as the solid becomes softer, but as the solid becomes too soft, the vanishing elasticity will result in a decreasing deformation at the contact line. Upon comparing deformations caused by 2-D and 3-D drops, we have found no qualitative difference in behaviour when changing γ/ER_0 .

Subsequently we have included the microscopic scale of molecular interactions, a , in our single drop model. Hereby we could capture the transition from Young's to Neumann's law in contact line geometry (Fig. 3.6), therefore allowing to calculate the complete contact line geometry as a function of γ/ER_0 (Fig. 3.9). With γ/E being the relevant length scale of deformations, we have shown that a drop on a soft solid exhibits two transitions when increasing γ/E : (i) Development of a Neumann-like cusp when γ/E reaches the order of molecular interactions a , and (ii) a solid body rotation of the contact line geometry when γ/E reaches the scale of the drop R_0 . Importantly, the first transition controlled by γ/Ea was shown to determine the contact angles at scale a . Any further increase of γ/E solely introduces a rotation of the system, but does not change the actual contact angles anymore.

In the last section we have calculated the changes in free energy as a function of γ/ER_0 (Fig. 3.11). We found that drops preferably locate themselves in regions of low stiffness, because the decrease in capillary liquid energy F_γ turned out to be dominant against any energy increase associated with the solid. This could therefore explain the observed durotaxis of drops that Style *et al* have shown in experiments [23].

Chapter 4

Drop Interactions

In this chapter we will calculate the forces of 2-D drop-drop interactions. In section 4.1 we start by extending the single drop model to a model that accounts for two droplets on a soft solid. Similar to the Cheerios effect, the local perturbations of one particle in the environment of another can lead to mutual attraction, such that an intermediate equilibrium state at some separation distance ℓ is not possible. Analogously, this suggests that introducing a second liquid drop on a soft solid changes the *static* problem of a single drop to a *dynamic* problem for two drops. Section 4.2 will discuss in detail how deal with this mutual interaction force, while still using a static description of the problem. Subsequently, section 4.3 gives the obtained numerical results, revealing the nature of drop-drop interactions on soft solids.

4.1 Extending the single drop model

A single drop on a soft solid has a stress distribution that is symmetric with respect to the drop's center. As such, the resulting surface deformations are symmetric with respect to its center, leading to a contact angle θ that is the same on both sides of the drop as in Fig. 3.2. By introducing a second drop, however, the drop is no longer a symmetry axis for the stress distribution. Instead, for two drops separated over a center to center distance ℓ , the vertical line $x = 0$ is now the symmetry axis as sketched in Fig. 4.1. As a result this can lead to asymmetric droplets sketched in Fig. 4.1, thereby inducing a bias in the inner and outer contact angle, named θ_{in} and θ_{out} respectively.

Moreover, when calculating drop-drop interactions it is important that we are looking at the

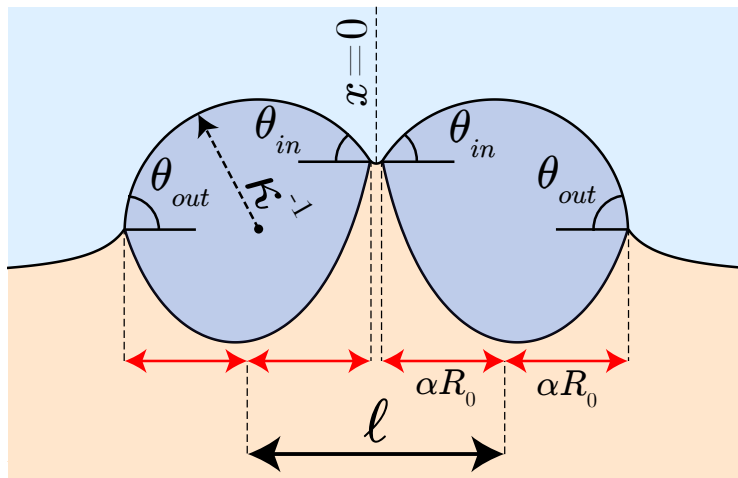


Figure 4.1: Schematics of two drops on a substrate, separated by a distance ℓ . Introducing a second drop results in a total stress distribution with respect to a drop's center that is no longer symmetric, causing the contact angles of the drop be different; $\theta_{out} \neq \theta_{in}$. The contact radius of the drop is scaled by factor α to ensure volume conservation.

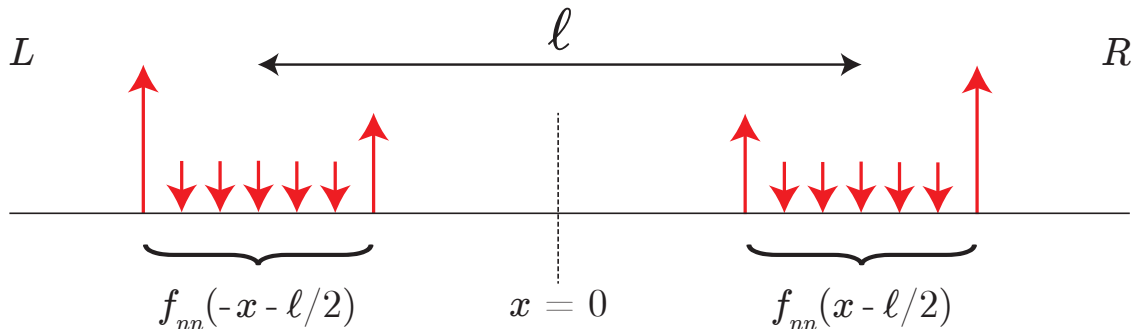


Figure 4.2: Sketch of the drop-on-solid stress distributions of both drops. If the drops are separated by a distance ℓ , the stress distribution of the right drop, R , is given by shifting Eq. (4.1) over a distance $\ell/2$. Mirroring the resulting function $f_{nn}(x - \ell/2)$ in the $x = 0$ plane provides the stress distribution of the left drop, L .

same physical system, *i.e.*, the same volume of liquid for all separation distances ℓ . Specifically, there is *a priori* no reason that the distance between the contact lines R_0 is constant upon varying ℓ , because elastic deformations of the substrate will change the shape of the drop. For now, it is sufficient to mention that we will scale the base radius of an undisturbed drop, R_0 , by a factor α in order to ensure constant drop volume. The factor α is a function of ℓ and remains to be determined numerically [Fig. 4.9(b)], such that drops of constant volume have an effective base radius of $R = \alpha(\ell)R_0$. Clearly, if $\ell \rightarrow \infty$ drops do not feel each other presence, such that we should retrieve undisturbed drop radius R_0 , in other words if $\ell \rightarrow \infty$ then $\alpha = 1$.

In short, introducing a second drop brings along some complications. We have seen above that these are (i) the drop is no longer a symmetry axis for the stress distribution, thus its contact angles no longer necessarily have to be the same, and (ii) the radius is no longer conserved due to droplet interaction. We incorporate both effects in the (dimensionless) stress distribution by generalizing Eq. (2.28) to (we set $\ell = 0$ for a moment and consider a single drop for convenience)

$$f_{nn}^D(x) = (\sin \theta_{in}) \delta(x + \alpha) + (\sin \theta_{out}) \delta(x - \alpha) - \kappa \Theta(\alpha - |x|), \quad (4.1)$$

with

$$\frac{1}{\kappa} = \frac{2\alpha}{\sin \theta_{in} + \sin \theta_{out}}. \quad (4.2)$$

Here the superscript D refers to the *double*-drop problem and for a derivation of the curvature κ [Eq. (4.2)] we refer to section 4.2.2. Using Eq. (4.1) we can write down the total stress distribution, $\sigma_{nn}^D(x)$, induced by a drop pair separated by a center-to-center distance ℓ . By symmetry arguments, the stress distribution of the left drop equals the stress distribution of the right drop, but mirrored in the $x = 0$ plane, as sketched in Fig. 4.2. Including the solid capillary pressure in the total stress, in analogy to the single drop, we obtain

$$\sigma_{nn}^D(x) = \frac{\gamma}{R_0} \left[\underbrace{f_{nn}^D(-x - \ell/2)}_{\text{left drop}} + \underbrace{f_{nn}^D(x - \ell/2)}_{\text{right drop}} + \frac{\gamma_S}{\gamma} \frac{d^2 h}{dx^2} \right]. \quad (4.3)$$

Note the difference with the stress distribution for a single drop [Eq. (3.1)] which is characterized by a single contact angle θ . In contrast, Eq. (4.3) depends on both θ_{in} and θ_{out} , because (i) normal tractions represented by the δ -functions in Eq. (4.1) both have a different prefactor dependent on the actual contact angle θ_{in} and θ_{out} and (ii) the liquid curvature κ is a function of both of these angles. Furthermore, note that the normal tractions in Eq. (4.1) now work at $x \pm \alpha$ and that Laplace pressure acts over a region $-\alpha < x < \alpha$, whereas the single drop problem simply had $\alpha = 1$.

Employing Eq. (4.3), the surface deformations follow from convoluting the stress function with the elastic kernel, such that

$$h^D(x) = \int_{-\infty}^{+\infty} dx' \sigma_{nn}^D(x') \mathcal{K}(x' - x). \quad (4.4)$$

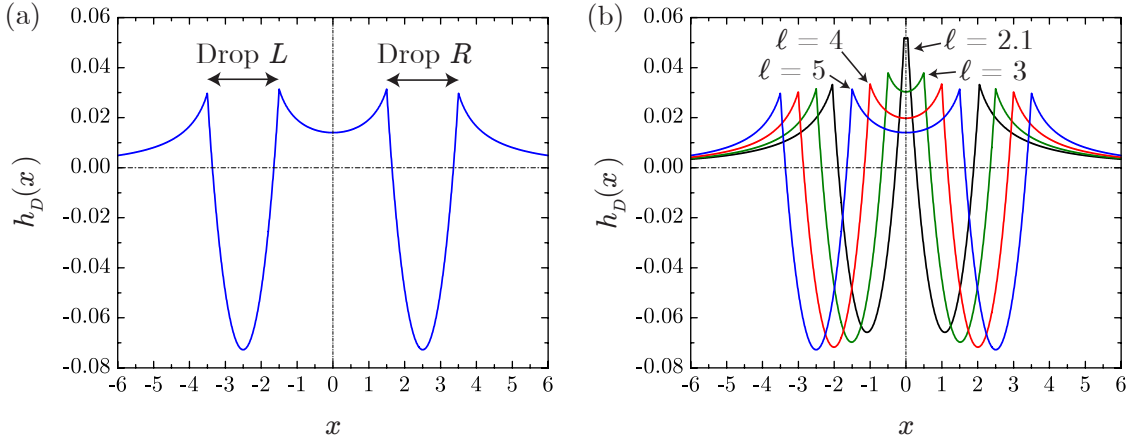


Figure 4.3: Calculated surface profiles, $h^D(x)$, obtained by solving Eq. (4.5), using $\gamma/\gamma_S = 0.3$ and $\gamma/ER_0 = 0.2$. (a) Surface profile for $\ell = 5$. The left and right drop are located at $-\alpha < x + \ell/2 < \alpha$ and $-\alpha < x - \ell/2 < \alpha$ with its contact lines at $x = -\ell/2 \pm \alpha$ and $x = \ell/2 \pm \alpha$, respectively. The value of α has a value close to 1, i.e. $\alpha \approx 1$. (b) Surface profiles for 4 different values of the separation distance ℓ . Note how the soft solid in between the drops is increasingly pulled up as the drops approach each other, while simultaneously the drop's center at $x = \ell/2$ is lifted.

Analogously to the single 2-D drop, we choose to solve Eq. (4.4) by using a FT. It can be shown that by taking the FT one obtains

$$\hat{h}^D(q) = \frac{\frac{3}{\sqrt{2\pi}} \frac{\gamma}{ER_0} e^{-iq\ell/2} [\hat{f}_{nn}^D(-q) + \hat{f}_{nn}^D(q)] \hat{\mathcal{K}}(q)}{1 + \frac{3}{\sqrt{2\pi}} \left(\frac{\gamma}{ER_0} \frac{\gamma_S}{\gamma} \right) q^2 \hat{\mathcal{K}}(q)}, \quad (4.5)$$

where we have calculated $\hat{f}_{nn}^D(q)$ as

$$\hat{f}_{nn}^D(q) = \frac{1}{\sqrt{2\pi}} \left[\kappa \frac{\sin(\alpha q)}{q} + (\sin \theta_{out}) e^{iq\alpha} + (\sin \theta_{in}) e^{-iq\alpha} \right].$$

Note that the separation distance ℓ appears in the numerator of Eq. (4.5). The FT of the kernel, $\mathcal{K}(x)$, was already given by Eq. (3.4). Similar to the previous chapter, the problem is now refined to finding the IFT of Eq. (4.5).

We have calculated $h^D(x)$ by calculating the IFT numerically: Fig. 4.3 shows the resulting surface profiles for a couple of different values of ℓ . Fig. 4.3(a) illustrates the presence of two drops. As for the single drop [Fig. 3.1], we observe stretching of the solid in the periphery of the contact lines and compression of the solid at the center of the drop. Note, however, the effect of a second drop: At the inner contact lines, separated by a relatively small distance, the combined normal tractions of both drops manage to pull the solid surface higher than at the outer contact lines. As a result, surface deformations are more pronounced in between the two drops leading to an asymmetry: The deformation at the inner contact lines is larger than that at the outer contact lines, which we will name h_{in} and h_{out} respectively. As the separation distance between the drops decreases, the asymmetry $h_{in} - h_{out}$ becomes more and more pronounced as illustrated in Fig. 4.3(b). In addition, note how the minima of $h^D(x)$ start to increase as the drops approach each other, which is a direct consequence of the additional normal tractions of the neighbouring drop.

While Fig. 4.3 shows the solid shapes, the liquid shapes remain to be determined. In fact, obtaining the exact solid shapes as shown above already required more work than the simple picture of just solving Eq. (4.5). The challenge lies in connecting the spherical caps $\mathcal{H}(x)$ to the surface profiles as shown above, because the interplay between solid and drop determines the values of θ_{in} and θ_{out} . For the single drop on a soft solid we have seen that the contact angle θ

was determined by the horizontal Neumann condition. As argued in the beginning of this chapter, however, it is expected that there is no equilibrium state at intermediate values of ℓ . This tells us that both contact angles can no longer be determined by a horizontal balance of stresses (Neumann) and that apparently other conditions should apply. In the next section will elaborate in detail on the conditions which determine the contact angles θ_{in} and θ_{out} .

4.2 Presence of a second drop: A non-equilibrium state

In chapter 2 we have seen that solving the elastic problem only was not sufficient to find the correct physical solution: The correct physical solution we were after was the one satisfying the horizontal Neumann condition for the contact angle. Therefore, we needed an iterative solving mechanism that resolves the elastic problem until horizontal Neumann was satisfied, see section 2.3. Since the single-drop problem had one free parameter, namely the contact angle θ , this allowed us to find a particular value for θ such that the system satisfied the horizontal Neumann condition [Fig. 2.4].

A priori one might have expected that the single-drop problem had two free parameters, namely the Lagrange multipliers P and λ . Requiring equilibrium of the liquid-vapor interface, however, resulted in only *one* independent multiplier, since P and λ are linearly dependent through $P = \lambda/R_0$. In other words, once $\lambda(\theta)$ is set through selecting θ , the Laplace pressure P is immediately determined and cannot be controlled. Effectively we thus have a single independent parameter, which is a function of θ in this case, allowing us to satisfy one condition, namely the horizontal Neumann condition.

At this point we expect we will need at least two independent parameters for the double drop problem, because drops can have distinct inner and outer contact angles. In fact, we will see below that we in addition need a third independent parameter which accounts for the non-equilibrium state the two drops are in.

4.2.1 A thought experiment: Fixing the drop separation ℓ

We will now place a second drop on the substrate as in Fig. (4.1), of identical volume and material properties. Introducing a second drop prevents the system from being in an equilibrium state due to drop-drop interactions so that there does not exist an equilibrium for an intermediate separation ℓ , in analogy to the Cheerios-effect. As such, we cannot simply find the equilibrium conditions for two drops separated by a distance ℓ anymore through energy minimization, as was done for a single drop in the previous chapter. Nonetheless, we can introduce some external horizontal force f_x to the system necessary to keep the drops separated by a distance ℓ . Let us assume this external force is applied by an experimentator in the three different possible ways sketched in Fig. 4.4, thereby holding the drops separated by a constant distance ℓ :

- (i) The experimentator pins the *outer* contact lines by exerting a horizontal force f_x at these contact lines, while the inner contact lines are free to equilibrate and satisfy the horizontal Neumann condition [Fig. 4.4(a)].

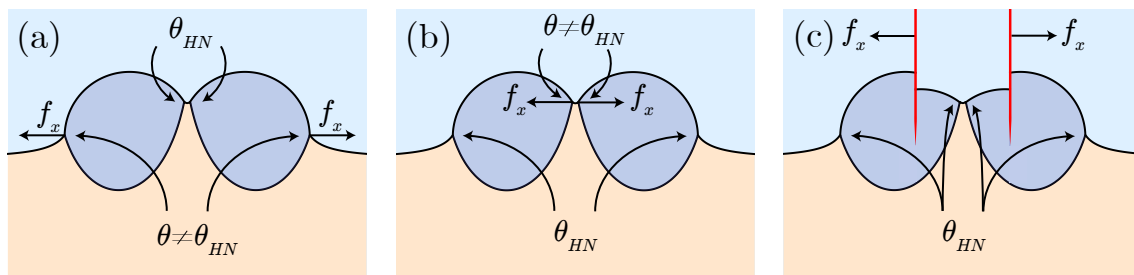


Figure 4.4: Holding the out-of-equilibrium drops at a fixed position in three different ways. In (a-c) we denote the local horizontal Neumann contact angle by θ_{HN} . (a) Pinning of the outer contact lines. (b) Pinning of the inner contact lines. (c) Holding the drops in place using a 2-D needle.

- (ii) The experimentator pins the *inner* contact lines by exerting a horizontal force f_x at these contact lines, while the outer contact angles are free to equilibrate and satisfy the horizontal Neumann condition [Fig. 4.4(b)].
- (iii) The experimentator holds each of the drops in place with a needle [Fig. 4.4(c)] exerting a horizontal force f_x , such that all the contact angles satisfy horizontal Neumann. For simplicity we assume the needle is wetted by a contact angle of $\pi/2$.

With the mechanical force f_x acting on the system there does exist an equilibrium. To investigate how this force can be computed in practice, we turn to a simpler example of a drop on a rigid substrate that presents a wettability gradient.

A sessile drop on a surface with a gradient in wettability: No equilibrium— A sessile drop on a partially wetting substrate is known to take the form of a spherical cap, having equilibrium contact angle equal to Young’s angle, θ_Y . If the same drop is now placed on a substrate having a linear gradient in wettability $\partial\gamma_{SL}(x)/\partial x = \text{constant} < 0$, the drop will translate on the substrate to lower its free energy and importantly, does not have an equilibrium state as displayed in Fig. 4.5(a). Hence, we have to exert a horizontal force to keep the drop at a steady position.

Here we first compute the force by pinning the right contact line by a force f_x . This means the right contact angle θ_R is not equal to Young’s angle $\theta_{R,Y}$, but that by contrast the left contact angle will equilibrate, $\theta_L = \theta_{L,Y}$. Therefore, the force f_x equals

$$f_x = \gamma \cos \theta_R - \gamma \cos \theta_{R,Y}. \quad (4.6)$$

By pinning the contact line the drop will take the shape of a perfect spherical cap, such that from geometry $\theta_R = \theta_{L,Y}$, allowing us to write

$$\begin{aligned} f_x &= \gamma \cos \theta_{L,Y} - \gamma \cos \theta_{R,Y} \\ &= [\gamma_{SV} - \gamma_{SL}(-R_0)] - [\gamma_{SV} - \gamma_{SL}(R_0)] \\ &= \gamma_{SL}(R_0) - \gamma_{SL}(-R_0) = -2R_0 \frac{\partial\gamma_{SL}}{\partial x}, \end{aligned} \quad (4.7)$$

where we have used Young’s relation to relate Young’s angle to the corresponding surface energies. While this approach assumes the total force f_x is localized at one of the contact lines, the result would be no different when calculating f_x from an energy approach. To see why, consider a virtual displacement of the drop over a distance dx as sketched in Fig. 4.5(b), yielding an energy change dE ,

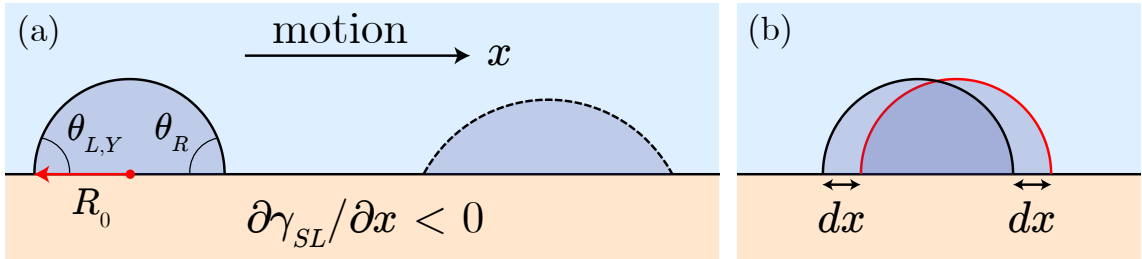


Figure 4.5: The translating and virtual displacement of a sessile drop on a surface with a gradient in wettability. (a) Sessile drop translating on a surface with a gradient in wettability. In order to lower its free energy the drop moves to the region of lower γ_{SL} , accordingly decreasing its contact angle θ while increasing its contact radius R_0 . Because the surface has a gradient in wettability, a freely moving drop has distinct contact angles, that is, $\theta_{L,Y} \neq \theta_R$. (b) Schematics of the virtual displacement of a drop on a surface with a gradient in wettability. Using this approach the energy change associated with a displacement dx is calculated, thereby providing us f_x .

$$\begin{aligned}
dE &= dx \left[\gamma_{SV} - \gamma_{SL}(-R_0) \right] + dx \left[\gamma_{SL}(R_0) - \gamma_{SV} \right] \\
&= dx \left[\gamma_{SL}(R_0) - \gamma_{SL}(-R_0) \right] \\
&= dx \left[2R_0 \frac{\partial \gamma_{SL}}{\partial x} \right]
\end{aligned} \tag{4.8}$$

Per definition, $f_x = -dE/dx$, such that the above result is identical to the result obtained in Eq. (4.7). Importantly, this suggests that calculating the force f_x through the imbalance at one of the contact lines is a valid method and that one does not need to prescribe the force f_x in any other form, for example a body force.

We will now use the same method to calculate f_x in the elastic problem, for the cases where we are pinning the contact line [Fig. 4.4(a,b)]. The interaction force f_x can be measured by calculating the imbalance of stresses at one of the contact lines numerically, that is

$$-f_x = \pm \left[\gamma \cos \theta + \gamma_S \cos \theta_{SL} - \gamma_S \cos \theta_{SV} \right] \quad [\text{Contact line pinning, Fig. 4.4(a,b)}] \tag{4.9}$$

where the + sign applies for inner contact line pinning and the – sign for outer contact line pinning. One could regard this force as representing the degree of deviation from horizontal Neumann, because $f_x = 0$ corresponds to a perfect balance of stresses. Determining f_x for the needle case [Fig. 4.4(c)], however, requires a slightly different approach. Inserting the needle results in a jump of the liquid height, $\Delta \mathcal{H}$, at the respective left and right sides of the needle, sketched in Fig. 4.6. The needle therefore effectively feels the Laplace pressure acting over a region $\Delta \mathcal{H}$, resulting in a force

$$-f_x = \Delta p \Delta \mathcal{H} \quad [\text{Needle, Fig. 4.4(c)}] \tag{4.10}$$

We included a minus sign in Eqs. 4.9 and 4.10 explicitly for f_x , because these are the interaction forces acting on the drop. By Newton's third law, however, the experimenter has to exert a force $+f_x$, opposite in sign, to keep the drops in place.

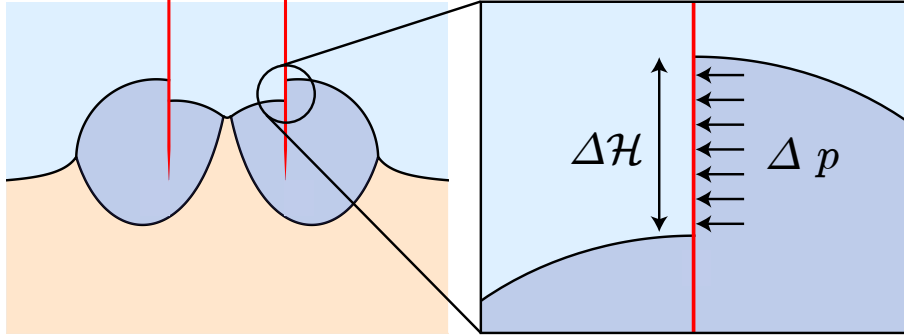


Figure 4.6: Holding the drops in place with a needle. The needle has wetting properties $\gamma_{SV} = \gamma_{SL}$ and protrudes the liquid surface at $d\mathcal{H}/dx = 0$. This ensures the drop shape is not altered beforehand already by the wetting properties of the needle. Nonetheless, by inserting the needle the liquid surface at the left and right side of the needle makes a jump, $\Delta \mathcal{H}$. The needle therefore effectively feels the Laplace pressure acting over a region $\Delta \mathcal{H}$, resulting in a force $f_x = -\Delta p \Delta \mathcal{H}$.

4.2.2 The liquid shape $\mathcal{H}(x)$ for asymmetric drops

At this point we have introduced the mechanical force f_x which ensures both drops are kept separated by a constant distance ℓ , and α , required to operate at constant drop volume V . Taking into account the distinct contact angles θ_{in} and θ_{out} for asymmetric drops, we have the following set of (independent) parameters associated with the double drop problem:

- (i) f_x
- (ii) θ_{in}
- (iii) θ_{out}
- (iv) α

Note that we excluded the Laplace pressure P ($= \Delta p$) as an independent parameter, because it couples directly to α , θ_{in} and θ_{out} , through $P = \gamma(\sin \theta_{in} + \sin \theta_{out})/(2\alpha R_0)$. With the 4 independent parameters mentioned above, we can satisfy the following 4 corresponding conditions:

- (i) $\theta_{in} = \theta_{HN}$ or $\theta_{out} = \theta_{HN}$
- (ii) $\mathcal{H}(x_{in}) = h(x_{in})$
- (iii) $\mathcal{H}(x_{out}) = h(x_{out})$
- (iv) $V = V_0 = \text{constant}$

Here x_{in} and x_{out} denote the respective positions of the inner and outer contact lines, while V_0 is the unperturbed single drop volume. Conditions (ii) and (iii) are simply a statement that the liquid surface should meet with the solid at these points for a contact line to exist, similar to the single drop problem where we imposed $\mathcal{H}(\pm R_0) = h(\pm R_0)$. Condition (i) reflects the two different scenarios for contact line pinning, sketched in Fig. 4.4(a,b), where only the inner or outer contact angles can satisfy the horizontal Neumann condition. Alternatively, holding the drops in place with a needle [Fig. 4.4(c)] results in both the inner and outer contact angles satisfying horizontal Neumann. This is directly related to the discontinuity $\Delta \mathcal{H}$ the liquid shape poses (Fig. 4.6), thereby introducing an additional independent parameter such that now both $\theta_{in} = \theta_{HN}$ and $\theta_{out} = \theta_{HN}$ can be satisfied.

The conditions mentioned above uniquely define the values of the corresponding parameters, such that we have hereby obtained closure of the elastic problem for two drops. We shall now proceed solving the actual equations for the liquid interface $\mathcal{H}(x)$.

Mathematical expression for the liquid surface, $\mathcal{H}(x)$ — We are looking for a spherical cap that coincides with both contact lines, having distinct contact angles θ_{in} and θ_{out} and center coordinate (x_c, y_c) . The equation $\mathcal{H}(x)$ satisfying these conditions is most easily derived in the following way: Any bias in contact angles will induce a shift in the horizontal center coordinate of the spherical cap, that is, the center x_c will not exactly coincide with the vertical axis y positioned halfway between the contact lines as sketched in [Fig. 4.7]. By exploiting this horizontal shift x_c we can write,

$$\left. \begin{aligned} \sin \theta_{in} &= \kappa(\alpha R_0 + x_c) \\ \sin \theta_{out} &= \kappa(\alpha R_0 - x_c) \end{aligned} \right\}. \quad (4.11)$$

Such that eliminating the curvature κ from these equations yields

$$x_c = \frac{\alpha R_0 (d_0 - 1)}{1 + d_0} \quad \text{with} \quad d_0 \equiv \frac{\sin \theta_{in}}{\sin \theta_{out}}. \quad (4.12)$$

Moreover, Eq. (A.3) also provides us the curvature of the spherical cap in terms of contact angles by eliminating x_c ,

$$\frac{1}{\kappa} = \frac{2\alpha R_0}{\sin \theta_{in} + \sin \theta_{out}}. \quad (4.13)$$

Note that we recover $x_c = 0$ and $\kappa^{-1} = R_0/\sin \theta$, if $\theta_{in} = \theta_{out} \equiv \theta$, corresponding to a perfectly symmetric spherical cap, identically to the single drop problem. The last step in defining the spherical cap is calculating the vertical center coordinate, y_c . If we utilize h_{in} as a starting point for the cap, then we can directly see from Fig. (4.7) that $\cos \theta_{in} = (h_{in} - y_c) \kappa$, yielding

$$y_c(h_{in}, \theta_{in}) = h_{in} - (\alpha R_0 + x_c) / \tan \theta_{in}, \quad (4.14)$$

but y_c could be equally defined by utilizing h_{out} as a starting point, such that

$$y_c(h_{out}, \theta_{out}) = h_{out} - (\alpha R_0 - x_c) / \tan \theta_{out}, \quad (4.15)$$

The resulting circle equation, intersecting both contact lines now follows as

$$(x - x_c)^2 + (\mathcal{H} - y_c)^2 = \kappa^{-2}, \quad (4.16)$$

such that the resulting cap equation is given by the positive root of Eq. (4.16). We can neglect the negative root, because it will turn out that only contact angles $\theta < \pi/2$ will occur in the problem we are solving. The solution for the liquid cap $\mathcal{H}(x)$ with center (x_c, y_c) then reads

$$\mathcal{H}(x, \alpha, \theta_{in}, \theta_{out}) = y_c + \sqrt{-x_c^2 + \kappa^{-2} + 2x_c x - x^2}, \quad -\alpha R_0 \leq x \leq \alpha R_0, \quad 0 \leq \{\theta_{in}, \theta_{out}\} \leq \frac{\pi}{2}$$

with

$$x_c = \frac{\alpha R_0 (d_0 - 1)}{1 + d_0} \quad \text{where} \quad d_0 \equiv \frac{\sin \theta_{in}}{\sin \theta_{out}}$$

$$\kappa^{-1} = \frac{2\alpha R_0}{\sin \theta_{in} + \sin \theta_{out}},$$

$$y_c(h_{in}, \theta_{in}) = h_{in} - (\alpha R_0 + x_c) / \tan \theta_{in}$$

(4.17)

Eq. (4.17) is valid in the cases where one of the contact lines is pinned [Fig. 4.4(a,b)]. For the case in which the experimentator is holding the drops with a needle, we have to redefine this equation slightly to account for the discontinuity $\Delta\mathcal{H}$ at $x = x_c$,

$$\begin{cases} \mathcal{H}(x, \alpha, \theta_{in}, \theta_{out}) & \text{if } x < x_c \\ \mathcal{H}(x, \alpha, \theta_{in}, \theta_{out}) + \Delta\mathcal{H} & \text{if } x > x_c \end{cases} \quad (4.18)$$

where $\Delta\mathcal{H}$ remains to be determined numerically. The discontinuity is per definition located at $x = x_c$, because we pertrude the liquid surface with a needle [Fig. 4.6] at the specific point $\mathcal{H}'|_{x=x_c} \equiv 0$.

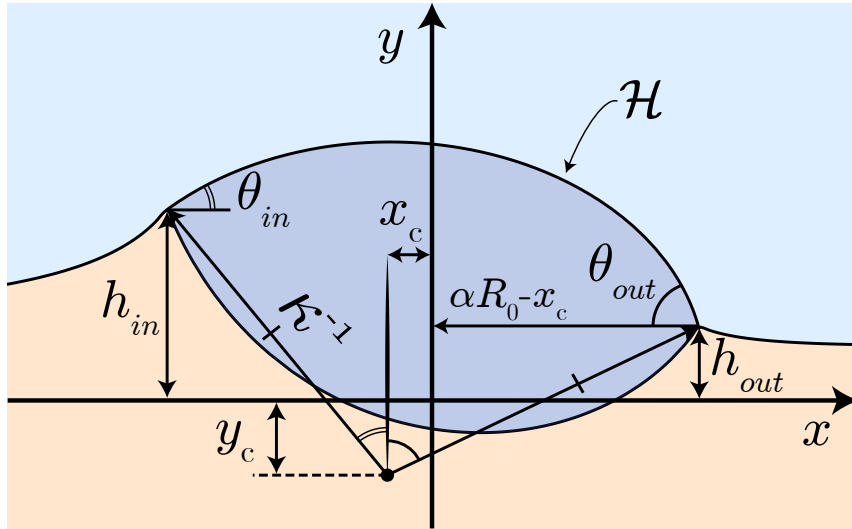


Figure 4.7: Definition of variables for an asymmetric drop. The second drop (not shown here) is located to the left of this drop thereby inducing drop asymmetry.

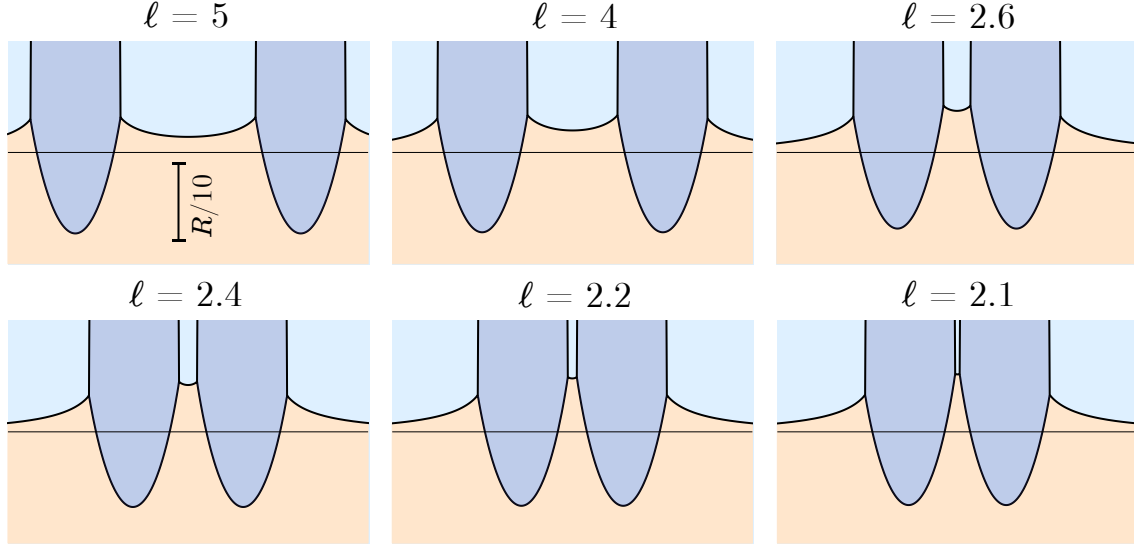


Figure 4.8: Surface profiles $h^D(x)$ with corresponding drops $\mathcal{H}(x)$ for decreasing separation ℓ , using $\gamma/\gamma_S = 0.3$ and $\gamma/ER_0 = 0.2$. To ensure equilibrium we have pinned the positions of the outer contact lines, while the inner ones satisfy horizontal Neumann, corresponding to the situation sketched in Fig. 4.4(a). In addition note how the soft solid in between the drops is increasingly pulled up as the drops approach each other.

We have illustrated the shapes of both the solid and liquid when pinning the outer contact lines in Fig. 4.8, where Eq. (4.17) was used to calculate the liquid shape. It should be realized that analogously to the single drop problem, the problem should be solved iteratively: Knowledge about the solid-vapor (θ_{SV}) and liquid-vapor (θ_{LV}) angles is required in order to verify the necessary conditions closing the problem. These angles, however, can only be known after solving the elastic problem [Eq. (4.4)] and hence knowing the solid shape, but its solution was already depend on θ_{in} and θ_{out} . We thus need a solving routine that resolves the elastic problem over and over, until all necessary conditions are satisfied. Below we discuss how we set up this (iterative) feedback mechanism, starting with a derivation of an exact relation between θ_{in} and θ_{out} .

Exact relation between θ_{in} and θ_{out} for contact line pinning— We have previously argued that the presence of a second drop induces an asymmetry, namely $h_{in} - h_{out} \neq 0$, also sketched in Fig. 4.7. As a result of this asymmetry the liquid cap connecting both contact lines has distinct contact angles, θ_{in} and θ_{out} . Earlier this section we have seen that the liquid cap requires two boundary conditions to be defined uniquely: Suppose we use h_{in} and θ_{in} as the boundary conditions. Because we have knowledge about the distance between the inner and outer contact lines, namely $2\alpha R_0$, this suggests we can directly calculate h_{out} and θ_{out} at the outer contact line. In other words, for a given $dh \equiv h_{in} - h_{out}$, θ_{in} and θ_{out} must be directly related through the asymmetry dh . This statement completely relies on the fact that the spherical cap $\mathcal{H}(x)$ is a *continuous* function that must coincide with both contact lines. As such, this statement is not valid if we are holding the drops with a needle since it poses a discontinuity $\Delta\mathcal{H}$. Nonetheless, it is valid when we are pinning the inner or outer contact lines as in Fig. 4.4(a,b) and then it might be shown that

$$\begin{aligned} \theta_{in}(\theta_{out}, dh, \alpha) &= \tan^{-1} \left[\frac{4\alpha^2 \tan \theta_{out} - dh(4\alpha + dh \tan \theta_{out})}{4\alpha^2 + dh(4\alpha \tan \theta_{out} - dh)} \right] \\ \theta_{out}(\theta_{in}, dh, \alpha) &= \tan^{-1} \left[\frac{4\alpha^2 \tan \theta_{in} + dh(4\alpha - dh \tan \theta_{in})}{4\alpha^2 - dh(dh + 4\alpha \tan \theta_{in})} \right] \end{aligned} \quad (4.19)$$

For a derivation of these equations we refer to appendix A. Again, note that if $dh \rightarrow 0$ and simultaneously $\alpha \rightarrow 1$, we retrieve the single drop configuration $\theta_{in} = \theta_{out} \equiv \theta$. The equations mentioned above are particularly useful for us, because if we impose the condition that the inner contact angle should equal θ_{HN} (horizontal Neumann), then we know beforehand already how

to pick the outer contact angle to ensure $\mathcal{H}(x_{cl,out}) = h(x_{cl,out})$. One could also rephrase it the other way around: Imposing horizontal Neumann for the outer contact angle through Eq. (4.19) allows to calculate the inner contact angle such that $\mathcal{H}(x_{cl,in}) = h(x_{cl,in})$. We should mention, however, that *a priori* the asymmetry dh already depends on the solution to the elastic problem, since $dh = dh(\theta_{in}, \theta_{out})$. Finding θ_{out} or θ_{in} through Eq. (4.19) therefore requires an iterative solving technique, discussed below. Nonetheless, these equations still provide us the best possible choice in a subsequent iteration step when one of the contact angles is given.

Double drop iteration scheme— For the double drop problem (Fig. 4.1) the central starting point is the stress distribution $\sigma^D(x, \theta_{\infty}, \theta_{out}, \alpha)$ which is convoluted with the elastic kernel $\mathcal{K}(x)$ in Eq. (4.4), yielding the solution for $h^D(x)$. In contrast to the single drop solving routine where we had to iterate to find one unknown parameter, we now have to iterate to find three unknown parameters: θ_{in} , θ_{out} and α . Assuming θ_{in} has to equal the Neumann angle, the solving technique for θ_{in} is no different from the single drop problem. Subsequently, the outer angle is found by employing the exact relation Eq. (4.19), providing an optimal choice for $\theta_{out,n+1}$. In the final step, the drop volume V will be calculated and compared to the volume of an undisturbed drop, say V_0 . Since it is expected the drop volume scales as $V \sim \alpha^2$, we pick $\alpha = \sqrt{V_0/V}$ in the subsequent iteration. Roughly three iterations a loop were necessary, i.e., 3 iterations for θ_{in} , θ_{out} and V to have a converged system.

4.3 Numerical results

In section 4.2.2 we have quantified the relevant independent parameters of the double drop problem: f_x , θ_{in} , θ_{out} and α . Using the numerical techniques discussed in the previous section, we will now calculate these parameters as function of the drop separation ℓ . Clearly, f_x is the most interesting parameter as it provides the force associated with drop-drop interactions. As anticipated we will find that f_x is identical for the three different cases sketched in Fig. 4.4. As such, we conclude that it is irrelevant to this problem where the force f_x exactly acts on the drop. All our numerical results have been calculated for $\gamma/\gamma_S = 0.3$ and $\gamma/ER_0 = 0.2$, unless mentioned otherwise.

We start by considering the degree of asymmetry involved in the problem by plotting $h_{in} - h_{out}$ as function of ℓ , which is a direct consequence of the second drop involved in the problem. In Fig. 4.3 we already observed from the separate surface profiles $h^D(x)$ that the asymmetry $dh = h_{in} - h_{out}$ became more pronounced as the drops approached each other. Indeed, Fig. 4.9(a) illustrates that the difference dh is increasing monotonically as the drops approach. From a physical point of view

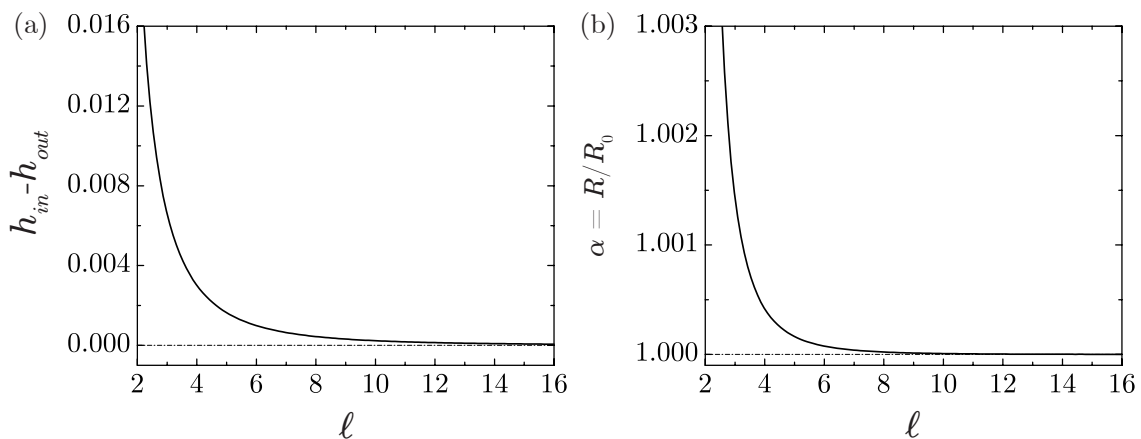


Figure 4.9: Results for $h_{in} - h_{out}$ and α , as a function of ℓ , calculated for $\gamma/\gamma_S = 0.3$ and $\gamma/ER_0 = 0.2$. We have obtained these results by pinning the outer contact lines, as sketched in Fig. 4.4(a). Results for the other cases are qualitatively the same and will not be shown here. (a) The asymmetry $h_{in} - h_{out}$ is increases monotonically as the drops approach. (b) The initial contact radius R_0 increases by factor α as the drops approach, to account for the otherwise decreasing volume.

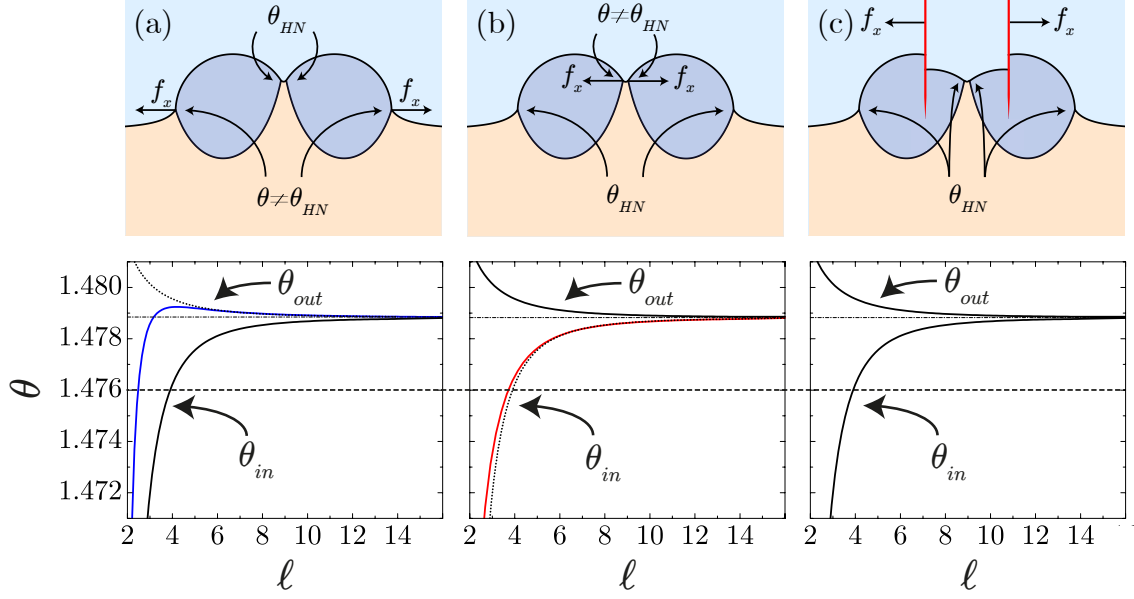


Figure 4.10: Dependence of the inner and outer contact angles as a function of the separation distance ℓ , when (a) Pinning the outer contact lines, (b) Pinning the inner contact lines, and (c) Holding the drops with a needle.

this can be explained by noting that for relatively small ℓ the inner contact lines of the drops are separated by such a small distance that the associated combined normal tractions manage to pull the solid surface together higher than the isolated outer contact lines manage to do. One could slightly quantify this idea by considering the stress distribution sketched in Fig. 4.2: For small ℓ the inner normal tractions of both drops are separated by a distance $\ell - 2\alpha$, while the inner and outer contact lines of *two different* drops (i.e. inner traction left drop, but outer traction right drop) are separated by a distance $\ell + 2\alpha$. (Recall that ℓ was non-dimensionalized by the drop radius R_0 , such that the 2α terms simply represent two drop radii). Upon comparing the ratio of the separation of contact lines, $(\ell + 2\alpha)/(\ell - 2\alpha)$, we see that the relative separation of contact lines becomes more and more important as $\ell \rightarrow 2$. As such, the relatively closely spaced inner normal tractions can together pull more efficiently on the solid than the relatively isolated outer contact lines can, thereby explaining the observed asymmetry. We note that the asymmetry $h_{in} - h_{out}$ approximately reaches 50% of the deformation of an individual drop, which is typically $h \sim 0.028$ for $\gamma/ER_0 = 0.2$.

Moreover, this asymmetry also causes the contact radius R_0 and the inner/outer contact angles to be altered as the drops approach each other. We readily explained in section 4.1 that we will scale the drop's contact radius by a factor α to ensure volume conservation. Figure 4.9 shows the necessary scaling factor to operate at constant volume V . It shows the effective contact radius αR_0 increases as the drops approach, thereby compensating for the otherwise decreasing volume in the unscaled problem.

The inner and outer contact angles as a function of ℓ are shown in Fig. 4.10. It shows the contact angles for all the three different scenarios, that is, when pinning the inner or outer contact line, or holding the drops separated by a needle. The black curves in all the panels of Fig. 4.10 represent the local Neumann angles. The solid blue line in panel (a) shows how θ_{out} behaves in order to ensure that $\mathcal{H}(x_{cl,out}) = h(x_{cl,out})$, while the solid red line in panel (b) shows how θ_{in} adapts such that $\mathcal{H}(x_{cl,in}) = h(x_{cl,in})$. The dotted black lines in panel (a) and (b) represent the local Neumann angles assuming horizontal Neumann would apply, but clearly the actual contact angles deviate from these dotted lines, thereby being responsible for an effective interaction force (inbalance of stresses).

Panel (a) illustrates the outer contact angle (blue line) in panel (a) displays a maximum. This maximum can be quantitatively explained as follows. As the drops are sufficiently separated ($\ell \gtrsim 6$) the inner contact line of the left drop and the outer contact line of the right drop effectively do

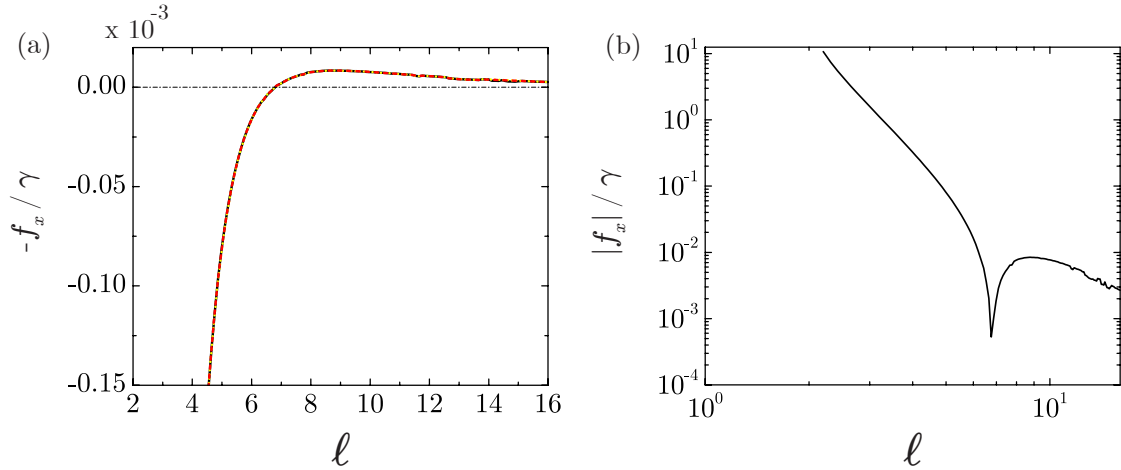


Figure 4.11: Mutual drop-drop interaction force f_x as a function of ℓ . (a) Results from the three different approaches sketched in Fig. 4.10, indicated by the red, black and yellow data. Importantly, note that these different approaches all result in the same f_x . Furthermore, we observe that there exists an equilibrium position for which $f_x = 0$, but it is an unstable ($\partial^2 f_x / \partial x^2 < 0$) equilibrium, however. (b) Absolute value of f_x on a log-log scale. Even though we cannot observe any power law behaviour in the far-field of ℓ due lack of numerical data, we expect that $f_x \sim \ell^{-5}$ based on a far-field expansion of the elastic energy.

barely feel each other. Hence, any asymmetry in the system has to be balanced by an increase in θ_{out} such that $\mathcal{H}(x_{cl,out}) = h(x_{cl,out})$. In other words, the solid needs to be increasingly stretched to make sure the solid coincides with the liquid cap. However, the competing effect is that as the drops become more closely ($\ell \lesssim 6$), the inner contact line of the left drop and the outer contact line of the right drop start to feel each other. From this point, the necessary stretching of the solid is taken over by the left drop and θ_{out} will accordingly decrease. Furthermore, we observe that upon comparing the Neumann angles (solid black lines) in panel (a-c), the Neumann angles in panel (a) and (b) look identical to those in panel (c). This suggests the inner and outer contact angles might be regarded as being decoupled, that is, a (small) change in θ_{in} does not change the elastic problem such that the obtained result for θ_{out} is altered (or the other way around).

It remains to discuss $f_x(\ell)$, the parameter which will directly provide us the force associated with drop-drop interactions. Calculating the force f_x allows to verify our hypothesis that it is unimportant where the force f_x is exactly acting on the drop: Indeed, the observed collapse in Fig. 4.11(a) shows that the force f_x for all the three different scenarios sketched in Fig. 4.10 is identical, as anticipated. Interestingly, the force f_x is non-monotonic in ℓ and displays a maximum around $\ell = 8$, suggesting at least two mechanisms are competing. Inspired by the single drop energy (Fig. 3.11), where the elastic and solid capillary energy terms were opposite in sign to the liquid capillary energy, we here expect f_x to be determined by the competition between the solid and liquid energy. We speculate that the short range attraction ($\ell \lesssim 8$) is dominated by the decrease in liquid capillary energy, which is supported by the significant drop asymmetry that sets in for $\ell \lesssim 8$ [Figs. 4.9 and 4.10].

The drop-drop problem should be completed in future by considering a full energy approach, such that the above described mechanism can be verified. With the work done in thesis, however, we have shown to be able to capture the drop-drop interactions and to calculate the magnitude of these forces.

4.4 Summary

In this chapter we have extended the single drop model to account for the presence of a second drop on the solid at distance ℓ . We found that the presence of a second drop can lead to a significant asymmetry in each drop, which is caused by the surface deformations due to the other drop (Figs. 4.3 and 4.9). As such, the Neumann angles cannot be satisfied at both contact lines

for intermediate values of the drop separation ℓ , changing the problem from a static to a dynamic one. We forced an equilibrium state, however, by introducing a mechanical force f_x , holding the drops separated by a constant distance ℓ .

We considered three different scenarios in order to oppose the drop-drop interaction force, either by pinning the inner/outer contact lines or by holding the drops in place with a needle (Fig. 4.4). Calculating f_x numerically as a function of ℓ has shown these three different approaches all resulted in the same drop-drop interaction force $-f_x$ [Fig. 4.11(a)], indicating that localizing f_x at a single contact line is a valid approach.

Interestingly, the interaction force f_x was found to display a maximum when the drops are spaced approximately 8 drop diameters apart ($\ell \approx 8$) (Fig. 4.11). It seems likely therefore, that drop-drop interactions are caused by at least two competing effects, speculated to be long-range repulsive elastic interactions in the far-field and short-range liquid capillary attractive interactions in the near-field. The expected liquid capillary dominated attraction in the near-field is supported by the significant drop asymmetry that sets in for $\ell \lesssim 8$ (Fig. 4.9), leading to a reduction of the liquid cap energy.

Chapter 5

Discussion and Outlook

In this final chapter we will reflect on the main findings of this thesis and subsequently discuss possible interesting future research.

5.1 Discussion

By coupling the action of capillary forces to elastic theory we have shown how a liquid drop deforms a soft solid, with the typical size of deformation given by the elasto-capillary length γ/E . Interestingly, we found that the solid deformation at the drop's contact line exhibits non-monotonic behaviour (Fig. 3.4) when increasing the softness parameter γ/ER_0 . Specifically, for elasto-capillary lengths $\gamma/E \ll R_0$ the solid is very rigid and the drop has difficulties in deforming the solid, such that resulting deformations are small. For elasto-capillary lengths $\gamma/E \gg R_0$, elasticity vanishes and the solid becomes too soft to resist any normal traction near the contact line, again resulting in small deformations. The latter situation is equal to a liquid lens floating on a liquid substrate, such as an oil drop floating on water. For intermediate values of γ/ER_0 (≈ 0.1), however, there exists a maximum deformation where the solid is soft enough to get deformed, but on the other hand strong enough to resist any normal traction.

In addition, we have compared the capillary and elastic energies for drops on surfaces as a function of stiffness. It was found that the energies have opposite signs, but that the dominant contribution comes from the liquid-vapor free energy. This energy decreases on softer substrates. This explains recent experiments on durotaxis [23], which demonstrated that liquid drops on surfaces with a stiffness gradient have the tendency to migrate towards softer regions.

A direct consequence of these elastic deformations is that the contact angle θ a liquid drop makes on a soft solid is no longer governed by Young's law, which is the classical result for rigid surfaces. Instead, with γ/E being the relevant length scale of deformations, we have found that γ/E should be compared to two length scales, each of them characterizing a transition in contact line geometry: (i) The *microscopic* scale of molecular interactions a , and (ii) the *macroscopic* length scale of the drop R_0 , illustrated in Fig. 3.9. Importantly, the first transition controlled by γ/Ea was shown to determine the actual geometry near the contact line at scale a through the development of a Neumann-cusp. The second transition, controlled by γ/ER_0 , only describes a solid body rotation of the contact line geometry without any change of the actual contact angles and since $R \gg a$ thus requires much softer surfaces. This transition is visible on the macroscopic scale R_0 , in contrast to the first transition which is only visible on the microscopic scale.

Moreover, we have extended the single drop model to take into account a *second* liquid drop on the same solid. Subsequently, we have shown these drops exhibit an effective interaction force f_x (Fig. 4.11), caused by elastic deformations of the solid – in analogy to the cheerios effect, where solid particles at a liquid interface can interact through interfacial deformations. Taking advantage of the single drop problem we know that deformations tend to go to zero in both the limit $\gamma/ER_0 \ll 1$ and $\gamma/ER_0 \gg 1$, such that one should operate at the intermediate regime of γ/ER_0 for drop-drop interactions to be strongest. For $\gamma/ER_0 = 0.2$ it was shown by varying the drop-drop separation ℓ that the interaction force f_x displays a maximum when the drops are spaced 8 drop diameters apart ($\ell \approx 8$) (Fig. 4.11). This suggests that drop-drop interactions are

determined by at least two competing effects, expected to be repulsive elastic interactions in the far-field and liquid capillary attractive interactions in the near-field. The expected liquid capillary dominated attraction in the near-field is supported by the significant drop asymmetry that sets in for $\ell \lesssim 8$ (Fig. 4.9), leading to a reduction of the liquid cap energy. This can be verified by considering a full energy approach of the problem, directly shifting the current discussion to that of future research.

5.2 Outlook

In this thesis we have considered drop-drop interactions from a mechanical point of view, since we calculated the mechanical force f_x . In order to identify the relevant mechanisms responsible for this interaction force one should calculate the energy changes associated with the solid and liquid independently, as function of ℓ . Hereby we can verify our proposed mechanism for the maximum that f_x displays, explained at the end of the discussion section. Up to now, we have only been able to perform the variational analysis for a single drop. We are currently exploring the energetic approach for the two drop problem, by which we expect to obtain a more complete picture of the drop-drop interactions.

Since it was shown that two drops exhibit an interaction force f_x , it would be a natural extension to consider the *dynamics* of drop-drop interactions. Two drops that are attracting or repelling each other will move on the solid surface while continuously deforming the solid. In practice, the process of this continuous deformation will dissipate energy in the elastic medium. One could choose to describe these drop-drop dynamics by employing a visco-elastic model, accounting for the energy dissipation associated with the movement of the drops on the solid. Moreover, it would be interesting to perform an experiment that shows two drops really do interact in practice. One could therefore perform experiments to study the drop motion in the regime where drop-drop interactions are the strongest, that is, picking the value of γ/ER_0 where deformations are maximum for some γ/γ_s . A possible difficulty is that the preparation of the elastic medium should be well controlled to ensure a smooth elastic surface. This is particularly important regarding the relatively small magnitude of f_x : If drops cannot move smoothly on the elastic medium their contact lines might easily get pinned, thereby preventing drop movement. Recent experiments reporting drop motion on soft solids show that this is indeed feasible [23].

Regarding the single drop theory, it would be interesting to consider drops with an equilibrium contact angle different from $\theta_Y = \pi/2$. In this thesis we have always considered drops with $\theta_Y = \pi/2$, because we have set $\gamma_{SV} = \gamma_{SL}$ for technical reasons. Choosing γ_S to be different in and outside the drop, *i.e.*, $\gamma_{SV} \neq \gamma_{SL}$, allows modelling of drops with higher and lower contact angles than $\theta_Y = \pi/2$. For example, setting $\gamma_{SV} > \gamma_{SL}$ would result in flatter drops (lower θ). Varying γ/ER_0 for flatter drops might change the relative energy changes associated with the solid and liquid energy, compared to those shown in Fig. 3.11. As a result this could qualitatively change the behaviour of drops preferably locating themselves in regions of lower stiffness [23]. Furthermore, one could question how the contact line geometry is altered upon varying γ/ER_0 for $\gamma_{SV} \neq \gamma_{SL}$.

A lower contact angle would also result in smaller normal tractions, $\gamma \sin \theta$, and a smaller Laplace pressure $\Delta p \sim \sin \theta$, such that accordingly surface deformations $h(x)$ become smaller. Apart from decreasing normal tractions for flatter drops, on the contrary, tangential tractions f_t will increase as the drops flatten [11, 13, 17, 18, 38]. In future research our model should be completed by including tangential tractions, in particular to be able to calculate how they exactly affect drop-drop interactions in the near-field. This could be done by using an elastic kernel for tangential deformations, similarly to the formalism used to calculate normal deformations.

Appendix A

Liquid cap equations

A.1 Spherical cap single drop

The goal is to find a spherical cap, \mathcal{H} , intersecting both contact lines while having contact angle θ . The radius of curvature for a single drop is given by

$$\kappa^{-1} = \frac{R_0}{\sin \theta}$$

The circle intersecting through both contact lines has center $(0, y_c)$, where y_c depends on the contact angle via $y_c = h_0 - R_0 \cos \theta = h_0 - R_0 \cot \theta$. Starting from the equation describing a circle, we find

$$x^2 + \left(\mathcal{H} + \frac{R_0}{\tan \theta} - h_0 \right)^2 = \left(\frac{R_0}{\sin \theta} \right)^2 \quad (\text{A.1})$$

Eq. (A.2) has two roots in $\mathcal{H}(x)$. In the problem we are solving only contact angles $\theta < \pi/2$ will occur, allowing us to take the positive root:

$$\mathcal{H}(x, \theta) = h_0 - \frac{R_0}{\tan \theta} + \sqrt{\left(\frac{R_0}{\sin \theta} \right)^2 - x^2}, \quad -R_0 \leq x \leq R_0, \quad 0 \leq \theta \leq \frac{\pi}{2}. \quad (\text{A.2})$$

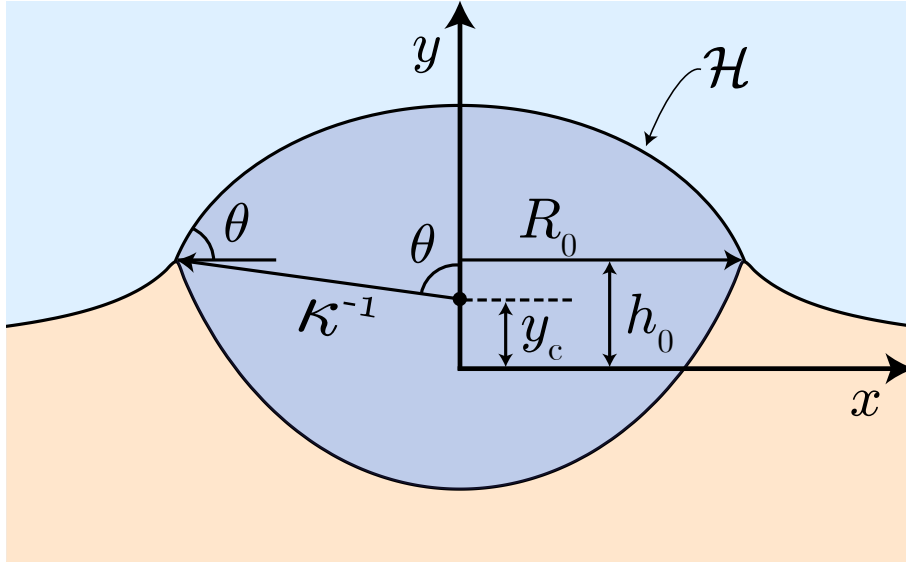


Figure A.1: Single drop schematics.

A.2 Relating θ_{in} to θ_{out} for contact line pinning

Similarly to problem dealing with the horizontal shift x_c [Eq. (A.3)], we can write for the vertical shift y_c

$$\left. \begin{aligned} \cos \theta_{in} &= \kappa (h_{in} - y_c) \\ \cos \theta_{out} &= \kappa (h_{out} - y_c) \end{aligned} \right\} \quad (\text{A.3})$$

Eliminating κ yields the vertical shift y_c ,

$$y_c(h_{in}, h_{out}, c_0) = \frac{h_{in} - c_0 h_{out}}{1 - c_0}, \quad \text{with } c_0 \equiv \frac{\cos \theta_{in}}{\cos \theta_{out}}, \quad (\theta_{in} \neq \theta_{out}). \quad (\text{A.4})$$

Apart from the above equation, we can also write y_c as

$$y_c(h_{out}, \theta_{out}) = h_{out} - (\alpha R_0 - x_c) / \tan \theta_{out}, \quad (\text{A.5})$$

Since we demand the spherical cap to intersect both contact lines, there should exist some relation between both contact angles. Equating Eqs.(4.15) and (A.5), and then solving for c_0 yields

$$c_0 = \frac{1 + x_c}{1 + x_c + \frac{dh \tan \theta_{in}}{R}}, \quad \text{with } dh = h_{out} - h_{in}. \quad (\text{A.6})$$

Since both $c_0 = c_0(\theta_{in}, \theta_{out})$ and $x_0 = x_0(\theta_{in}, \theta_{out})$, we are now in a position to express θ_{in} in terms of θ_{out} , or the other way around, through:

$$\begin{aligned} \theta_{in}(\theta_{out}, dh, \alpha) &= \tan^{-1} \left[\frac{4\alpha^2 \tan \theta_{out} - dh(4\alpha + dh \tan \theta_{out})}{4\alpha^2 + dh(4\alpha \tan \theta_{out} - dh)} \right] \\ \theta_{out}(\theta_{in}, dh, \alpha) &= \tan^{-1} \left[\frac{4\alpha^2 \tan \theta_{in} + dh(4\alpha - dh \tan \theta_{in})}{4\alpha^2 - dh(dh + 4\alpha \tan \theta_{in})} \right] \end{aligned} \quad (\text{A.7})$$

This relation tells us that once we have specified both h_{in} and h_{out} , and one of the contact angles, then the other contact angle will be fixed according to relation 4.19.

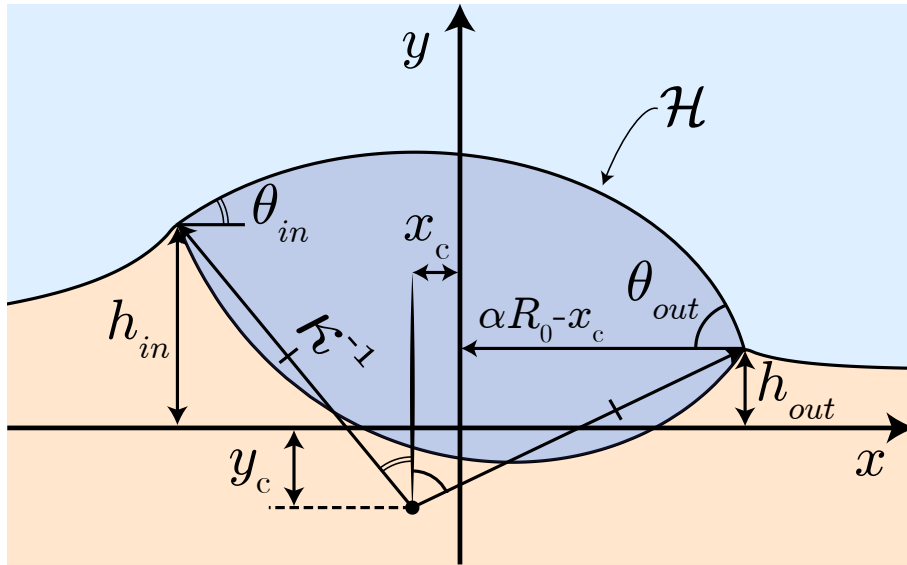


Figure A.2: Definition of variables for an asymmetric drop. The second drop (not shown here) is located to the left of this drop thereby inducing drop asymmetry.

Appendix B

Energy integrals

In any derivation below, we are using the following Fourier transform convention:

$$\mathcal{F}[f(x)] = \hat{f}(q) = \frac{1}{\sqrt{2\pi}} \int f(x) e^{-iqx} dx, \quad \mathcal{F}^{-1}[\hat{f}(q)] = f(x) = \frac{1}{\sqrt{2\pi}} \int \hat{f}(q) e^{iqx} dq.$$

B.1 Elastic energy

The internal elastic energy, E_{el} , stored in the bulk of an elastic medium can be calculated by carrying out a volume integral of the product of stress and strain,

$$W = \frac{1}{2} \int dV (\sigma_{ij} \epsilon_{ij}) \quad (\text{B.1})$$

The goal of the derivation below will be to express this volume integral in terms of an surface integral, which is possible in the case body forces, \vec{f} , are absent. We will start by calculating the work, U , done by surface tractions, \vec{T}_i , and subsequently show this equals the internal elastic energy. If surface tractions yield a deformation \vec{u} , then

$$\begin{aligned} U &= \frac{1}{2} \int dS T_i u_i = \frac{1}{2} \int dS \sigma_{ij} n_j \cdot u_i \\ &= \frac{1}{2} \int dV \frac{\partial}{\partial x_j} (\sigma_{ij} u_i) \\ &= \frac{1}{2} \int dV \left(\frac{\partial \sigma_{ij}}{\partial x_j} u_i \right) + \frac{1}{2} \int dV \left(\sigma_{ij} \frac{\partial u_i}{\partial x_j} \right), \end{aligned} \quad (\text{B.2})$$

where we have used Gauss' theorem to convert a surface integral to a volume integral. Per definition we have

$$\frac{\partial \sigma_{ij}}{\partial x_j} = \vec{\nabla} \cdot \vec{\sigma} \quad \text{and} \quad \vec{\nabla} \cdot \vec{\sigma} = -\vec{f},$$

where \vec{f} represent body forces. If we in addition define

$$\sigma_{ij} \frac{\partial u_i}{\partial x_j} = \sigma_{ij} \epsilon_{ij} \quad \text{with} \quad \epsilon_{ij} = \frac{1}{2} \left(\frac{\partial u_i}{\partial x_j} + \frac{\partial u_j}{\partial x_i} \right),$$

then we can write

$$U = \underbrace{\frac{1}{2} \int dV (-f_i u_i)}_{\text{Work by body forces}} + \underbrace{\frac{1}{2} \int dV (\sigma_{ij} \epsilon_{ij})}_{\text{Internal elastic energy}} \quad (\text{B.3})$$

In our case body forces are absent, such that $f_i = 0$. We therefore find that the work done by surface stresses equals the internal elastic energy, $U = E_{el}$:

$$\boxed{\frac{1}{2} \int dS T_i u_i = \frac{1}{2} \int dV (\sigma_{ij} \epsilon_{ij})} \quad (\text{B.4})$$

In the problem of a single drop on a soft solid, we consider only normal forces. Hence, the only contributions come from $T_n = f_{nn}(x)$ and $u_n = h(x)$. In principle $h(x)$ can be found by the IFT of Eq. (3.3), but if one wants to integrate $f_{nn}h(x)$ over the complete surface ranging from $-\infty < x < \infty$, one should accordingly carry out the IFT over the same range. It is therefore much more convenient to express the elastic energy as an Fourier integral, since we have the exact solution for $\hat{h}(q)$ [Eq. (3.3)]. We rewrite the elastic energy in terms of Fourier transforms below, where we note from Eq. 2.24 that using $T_n = f_{nn}(x)$ automatically includes the solid capillary energy F_S ,

$$\begin{aligned} F_{el} + F_S &= \frac{1}{2} \int dx f_{nn}(x) h(x) \\ &= \frac{1}{2} \int dx f_{nn}(x) \int dy \sigma_{nn}(y) \mathcal{K}(x-y) \\ &= \frac{1}{2} R_0 \frac{\gamma}{R_0} \int d\tilde{x} \tilde{f}_{nn}(\tilde{x}) \left(R_0 \frac{\gamma}{R_0} \frac{3}{2\pi E} \int d\tilde{y} \tilde{\sigma}_{nn}(\tilde{y}) \tilde{\mathcal{K}}(\tilde{x}-\tilde{y}) \right) \\ &= \frac{1}{2} \frac{3\gamma^2}{2\pi E} \int d\tilde{x} \left(\frac{1}{\sqrt{2\pi}} \int \hat{f}_{nn}(q) e^{iq\tilde{x}} dq \right) \left(\frac{1}{\sqrt{2\pi}} \int dq' \sqrt{2\pi} \hat{\sigma}_{nn}(q') \hat{\mathcal{K}}(q') e^{iq'\tilde{x}} \right) \\ &= \frac{3\gamma^2}{4\pi\sqrt{2\pi E}} \iint dq dq' \hat{f}_{nn}(q) \hat{\sigma}_{nn}(q') \hat{\mathcal{K}}(q') \int d\tilde{x} e^{i(q+q')\tilde{x}} \\ &= \frac{3\gamma^2}{4\pi\sqrt{2\pi E}} \iint dq dq' \hat{f}_{nn}(q) \hat{\sigma}_{nn}(q') \hat{\mathcal{K}}(q') 2\pi \delta(q+q') \\ &= \frac{3\gamma^2}{2\sqrt{2\pi E}} \int dq \hat{f}_{nn}(q) \hat{\sigma}_{nn}(-q) \hat{\mathcal{K}}(-q) \end{aligned}$$

We calculate the non-dimensional energy,

$$\boxed{\frac{F_{el}}{\gamma R_0} = \frac{3}{2\sqrt{2\pi}} \left(\frac{\gamma}{ER_0} \right) \int dq \hat{f}_{nn}(q) \hat{\sigma}(-q) \hat{\mathcal{K}}(q)} \quad (\text{B.5})$$

B.2 Solid surface capillary energy

The capillary energy associated with the solid surface tension can be calculated through

$$E_S = \gamma_S \int dx \sqrt{1 + \left| \frac{\partial h}{\partial x} \right|^2}. \quad (\text{B.6})$$

In the small slope approximation, $\left| \frac{dh}{dx} \right|^2 \ll 1$, the square root can be expanded to leading order in x as

$$\sqrt{1 + \left| \frac{dh}{dx} \right|^2} \approx 1 + \frac{1}{2} \left| \frac{\partial h}{\partial x} \right|^2. \quad (\text{B.7})$$

Substituting this result in Eq. (B.6) reads

$$E_S \approx \gamma_S \int dx + \frac{1}{2} \gamma_S \int dx \left| \frac{\partial h}{\partial x} \right|^2. \quad (\text{B.8})$$

One could recognize the first integral term in the above equation as being the unperturbed flat surface, while the second term represents the additional surface area created by any surface perturbations. Since we are interested in energy changes, we simply remove the (constant) offset

$\gamma_s \int dx$. As for the elastic energy, it is again much more convenient to express the solid surface capillary energy by an integral in Fourier space. One can hereby circumvent the necessary IFT required to obtain dh/dx . We rewrite the solid surface capillary energy in terms of Fourier transforms below,

$$\begin{aligned}
F_S &= \frac{1}{2} \gamma_s \int dx \left| \frac{\partial h}{\partial x} \right|^2 \\
&= \frac{1}{2} \gamma_s R_0 \int d\tilde{x} \left| \frac{\partial \tilde{h}}{\partial \tilde{x}} \right|^2 \\
&= \frac{1}{2} \gamma_s R_0 \int d\tilde{x} \left| \frac{1}{\sqrt{2\pi}} \int iq \hat{h}(q) e^{iq\tilde{x}} dq \right|^2 \\
&= \frac{1}{2} \gamma_s R_0 \int d\tilde{x} \left(\frac{1}{\sqrt{2\pi}} \int dq iq \hat{h}(q) e^{iq\tilde{x}} \right) \left(\frac{1}{\sqrt{2\pi}} \int dq' (-i) q' \overline{\hat{h}(q')} e^{-iq'\tilde{x}} \right) \\
&= \frac{1}{2} \frac{1}{2\pi} \gamma_s R_0 \iint dq dq' qq' \hat{h}(q) \overline{\hat{h}(q')} \int d\tilde{x} e^{i(q-q')\tilde{x}} \\
&= \frac{1}{2} \frac{1}{2\pi} \gamma_s R_0 \iint dq dq' qq' \hat{h}(q) \overline{\hat{h}(q')} \int d\tilde{x} e^{iq'\tilde{x}} e^{-iq\tilde{x}} \\
&= \frac{1}{4\pi} \gamma_s R_0 \iint dq dq' qq' \hat{h}(q) \overline{\hat{h}(q')} \sqrt{2\pi} \mathcal{F} [1 \cdot e^{iq'\tilde{x}}] \\
&= \frac{1}{4\pi} \gamma_s R_0 \iint dq dq' qq' \hat{h}(q) \overline{\hat{h}(q')} \sqrt{2\pi} \sqrt{2\pi} \delta(q - q') \\
&= \frac{1}{2} \gamma_s R_0 \int dq q^2 \hat{h}(q) \overline{\hat{h}(q)} \\
&= \frac{1}{2} \gamma_s R_0 \int dq q^2 \left| \hat{h}(q) \right|^2
\end{aligned}$$

We calculate the non-dimensional energy,

$$\boxed{\frac{F_S}{\gamma R_0} = \frac{1}{2} \left(\frac{\gamma_s}{\gamma} \right) \int dq q^2 \left| \hat{h}(q) \right|^2} \tag{B.9}$$

Bibliography

- [1] Pierre-Gilles De Gennes, Françoise Brochard-Wyart, and David Quéré. *Capillarity and wetting phenomena: drops, bubbles, pearls, waves*. Springer, 2004.
- [2] Kun Joong Park and Ho-Young Kim. Bending of floating flexible legs. *Journal of Fluid Mechanics*, 610:381–390, 2008.
- [3] Dominic Vella. Floating objects with finite resistance to bending. *Langmuir*, 24(16):8701–8706, 2008.
- [4] B Roman and J Bico. Elasto-capillarity: deforming an elastic structure with a liquid droplet. *Journal of Physics: Condensed Matter*, 22(49):493101, 2010.
- [5] Xiaoying Guo, Huan Li, Bok Yeop Ahn, Eric B Duoss, K Jimmy Hsia, Jennifer A Lewis, and Ralph G Nuzzo. Two-and three-dimensional folding of thin film single-crystalline silicon for photovoltaic power applications. *Proceedings of the National Academy of Sciences*, 106(48):20149–20154, 2009.
- [6] Ned Bowden, Insung S Choi, Bartosz A Grzybowski, and George M Whitesides. Mesoscale self-assembly of hexagonal plates using lateral capillary forces: synthesis using the capillary bond. *Journal of the American Chemical Society*, 121(23):5373–5391, 1999.
- [7] José Bico, Benoit Roman, Loïc Moulin, and Arezki Boudaoud. Adhesion: Elastocapillary coalescence in wet hair. *Nature*, 432(7018):690–690, 2004.
- [8] C Duprat, S Protiere, AY Beebe, and HA Stone. Wetting of flexible fibre arrays. *Nature*, 482(7386):510–513, 2012.
- [9] Charlotte Py, Paul Reverdy, Lionel Doppler, José Bico, Benoît Roman, and Charles N Baroud. Capillary origami: spontaneous wrapping of a droplet with an elastic sheet. *Physical review letters*, 98(15):156103, 2007.
- [10] Ramón Pericet-Cámara, Andreas Best, Hans-Jurgen Butt, and Elmar Bonaccorso. Effect of capillary pressure and surface tension on the deformation of elastic surfaces by sessile liquid microdrops: An experimental investigation. *Langmuir*, 24(19):10565–10568, 2008.
- [11] Joost H. Weijs. *Nanobubbles and Nanodrops*. Joost H. Weijs, 2013.
- [12] Elizabeth R Jerison, Ye Xu, Larry A Wilen, and Eric R Dufresne. Deformation of an elastic substrate by a three-phase contact line. *Physical review letters*, 106(18):186103, 2011.
- [13] Siddhartha Das, Antonin Marchand, Bruno Andreotti, and Jacco H Snoeijer. Elastic deformation due to tangential capillary forces. *Physics of Fluids*, 23:072006, 2011.
- [14] Robert W Style and Eric R Dufresne. Static wetting on deformable substrates, from liquids to soft solids. *Soft Matter*, 8(27):7177–7184, 2012.
- [15] Antonin Marchand, Siddhartha Das, Jacco H Snoeijer, and Bruno Andreotti. Contact angles on a soft solid: from youngs law to neumanns law. *Physical review letters*, 109(23):236101, 2012.

- [16] Robert W Style, Rostislav Boltyskiy, Yonglu Che, JS Wettlaufer, Larry A Wilen, and Eric R Dufresne. Universal deformation of soft substrates near a contact line and the direct measurement of solid surface stresses. *Physical review letters*, 110(6):066103, 2013.
- [17] Joost H Weijs, Bruno Andreotti, and Jacco H Snoeijer. Elasto-capillarity at the nanoscale: on the coupling between elasticity and surface energy in soft solids. *arXiv preprint arXiv:1303.6779*, 2013.
- [18] Antonin Marchand, Siddhartha Das, Jacco H Snoeijer, and Bruno Andreotti. Capillary pressure and contact line force on a soft solid. *Physical Review Letters*, 108(9):094301, 2012.
- [19] Antonin Marchand, Joost H Weijs, Jacco H Snoeijer, and Bruno Andreotti. Why is surface tension a force parallel to the interface? *American Journal of Physics*, 79:999, 2011.
- [20] Alain Carré, Jean-Claude Gastel, and Martin ER Shanahan. Viscoelastic effects in the spreading of liquids. 1996.
- [21] Joseph Antoine Ferdinand Plateau. *Statique expérimentale et théorique des liquides soumis aux seules forces moléculaires*, volume 2. Gauthier-Villars, 1873.
- [22] Serge Mora, Ty Phou, Jean-Marc Fromental, Len M Pismen, and Yves Pomeau. Capillarity driven instability of a soft solid. *Physical review letters*, 105(21):214301, 2010.
- [23] Robert W Style, Yonglu Che, Su Ji Park, Byung Mook Weon, Jung Ho Je, Callen Hyland, Guy K German, Michael Power, Larry A Wilen, John S Wettlaufer, et al. Patterning droplets with durotaxis. *arXiv preprint arXiv:1304.4277*, 2013.
- [24] Dominic Vella and L Mahadevan. The cheerios effect. *American journal of physics*, 73:817, 2005.
- [25] Manoj K Chaudhury and George M Whitesides. How to make water run uphill. Technical report, DTIC Document, 1992.
- [26] Chun-Min Lo, Hong-Bei Wang, Micah Dembo, and Yu-li Wang. Cell movement is guided by the rigidity of the substrate. *Biophysical journal*, 79(1):144–152, 2000.
- [27] Dennis E Discher, Paul Janmey, and Yu-li Wang. Tissue cells feel and respond to the stiffness of their substrate. *Science*, 310(5751):1139–1143, 2005.
- [28] Lorenzo Botto, Eric P Lewandowski, Marcello Cavallaro, and Kathleen J Stebe. Capillary interactions between anisotropic particles. *Soft Matter*, 8(39):9957–9971, 2012.
- [29] LD Landau. Em lifshitz theory of elasticity. *Course of theoretical physics*, 7, 1986.
- [30] Kenneth Langstreth Johnson and K Kenneth Langstreth Johnson. *Contact mechanics*. Cambridge university press, 1987.
- [31] Ramon Pericet-Camara, Günter K Auernhammer, Kaloian Koynov, Simone Lorenzoni, Roberto Raiteri, and Elmar Bonaccorso. Solid-supported thin elastomer films deformed by microdrops. *Soft Matter*, 5(19):3611–3617, 2009.
- [32] Laurent Limat. Straight contact lines on a soft, incompressible solid. *The European Physical Journal E*, 35(12):1–13, 2012.
- [33] Jerry B Marion and Stephen T Thornton. *Classical dynamics of particles and systems*. Saunders College Pub., 1995.
- [34] James Stewart. *Single variable calculus: early transcendentals*. Brooks/Cole Publishing Company, 2011.
- [35] Didier Long, Armand Ajdari, and Ludwik Leibler. How do grafted polymer layers alter the dynamics of wetting? *Langmuir*, 12(6):1675–1680, 1996.

- [36] Alexander D Poularikas. *Transforms and applications handbook*. CRC Press, 2010.
- [37] George Brown Arfken, Hans-Jurgen Weber, and Lawrence Ruby. *Mathematical methods for physicists*, volume 6. Academic press New York, 1985.
- [38] Joost H Weijs, Jacco H Snoeijer, and Bruno Andreotti. Capillarity of soft amorphous solids: a microscopic model for surface stress. *arXiv preprint arXiv:1310.3941*, 2013.